

Muhammad Sahimi · M. Reza Rahimi Tabar ·  
Alireza Bahraminasab · Reza Sepehrinia · S. M. Vaez Allaei

## Propagation and localization of acoustic and elastic waves in heterogeneous materials: renormalization group analysis and numerical simulations

Received: 8 November 2008 / Published online: 24 April 2009  
© Springer-Verlag 2009

**Abstract** We describe and discuss the recent progress in the study of propagation and localization of acoustic and elastic waves in heterogeneous media. The heterogeneity is represented by a spatial distribution of the local elastic moduli. Both randomly distributed elastic moduli as well as those with long-range correlations with a nondecaying power-law correlation function, are considered. The motivation for the study is twofold. One is that recent analysis of experimental data for the spatial distribution of the elastic moduli of rock indicated that the distribution is characterized by the type of long-range correlations that we consider in this study. The second motivation for the problem is to understand whether localization of electrons (which, in quantum mechanics, are described by wave functions) has any analogy in the propagation of classical waves in disordered media. The problem is studied by two approaches. One of them is based on developing a dynamic renormalization group (RG) approach to analytical analysis of the governing equations for wave propagation. The RG analysis indicates that, depending on the type of the disorder (correlated vs. uncorrelated), one may have a transition between localized and extended regimes in *any* spatial dimension. The second approach utilizes numerical simulations of the governing equations in two- and three-dimensional media. The results obtained by the two approaches are in agreement with each other. Using numerical simulations, we also describe how the characteristics of a propagating wave may be used for probing the differences between heterogeneous media with short- and long-range correlations. To do so, we study the evolution of several distinct characteristics of the waves, such as the amplitude of the coherent wave front, its width, the spectral densities, the scalogram (wavelet transformation of the waves' amplitudes at different scales and times), and the dispersion relation. It is demonstrated that such properties have completely different characteristics in uncorrelated and correlated media. Finally, it is shown how wave propagation may be used for establishing a link between the static and dynamical properties of heterogeneous media.

---

M. Sahimi (✉)  
Mork Family Department of Chemical Engineering and Materials Science, University of Southern California,  
Los Angeles, CA 90089-1211, USA  
E-mail: moe@iran.usc.edu; moe@usc.edu

M. R. Rahimi Tabar · R. Sepehrinia  
Department of Physics, Sharif University of Technology, 11155-9161 Tehran, Iran

M. R. Rahimi Tabar  
Institute of Physics, Carl von Ossietzky University, 26111 Oldenburg, Germany

A. Bahraminasab  
Department of Physics, Lancaster University, Lancaster LA1 4YB, UK

S. M. Vaez Allaei  
Department of Physics, University of Tehran, 14395-547 Tehran, Iran

## 1 Introduction

Wave propagation in heterogeneous media is a fundamental phenomenon of great scientific and practical interest, and has been studied for a long time. It is relevant to such important problems as analyzing seismic data for earthquakes and making predictions for their possible occurrence in the future, detecting underground nuclear explosions, understanding the large-scale structure of oil, gas, and geothermal reservoirs, gaining insight into what happens at large depths in the oceans, and designing instruments for medical imaging, as well as characterizing materials [1,2]. For example, seismic wave propagation and reflection are used to not only estimate the hydrocarbon content of a potential oil reservoir, but also the spatial distributions of its fractures, faults, and strata, as well as its porosity [3,4]. More generally, they are used to image structures located over a wide area, ranging from the Earth's near surface to the deeper crust and upper mantle.

The purpose of the present paper is to summarize the results of recent studies of wave propagation in heterogeneous media, which have attempted to elucidate the effect of strong heterogeneities, represented by a broad spatial distribution of the local elastic constants, on wave propagation in disordered media. An important example of such media is rock, which represents a highly heterogeneous natural material. Recently, extensive experimental data for the spatial distributions of the local elastic moduli, the densities, and the wave speeds in several large-scale porous rock formations, both off- and onshore, were analyzed [5]. The analysis indicated [5] the existence of long-range correlations in the spatial distributions of the measured quantities, characterized by *nondecaying power-law correlation functions*. The analysis provided an impetus for the present study and motivated an important question that we address in the present paper: How do such large-scale and strong heterogeneities affect wave propagation in elastic media, and in particular natural rock?

A second motivation for studying wave propagation in disordered media is provided by a well-known phenomenon in condensed matter physics, namely, the nature of electronic states in heterogeneous materials [6]. It is now well-understood that the answer to question of whether electrons in a given material are localized or are in an extended state depends strongly on the material's spatial dimensionality  $d$  and the state of its heterogeneity. In one-dimensional (1D) materials, even weak disorder, irrespective of the energy, localizes the wave function [7,8] and, therefore, the material is insulating. The envelope of the wave function  $\psi(\mathbf{x})$  decays at large distances  $|\mathbf{x}|$  from the domain's center as,

$$\psi(\mathbf{x}) \sim \exp[-|\mathbf{x}|/\xi(\omega)], \quad (1)$$

where  $\xi$  is the localization length at frequency  $\omega$ . In fact, the scaling theory of localization [9] predicts that, for  $d \leq 2$ , all the electronic states are localized (the material is insulating) for any degree of disorder, but a transition to extended states occurs for  $d > 2$ , depending on the strength of the disorder. The transition between the two states—the *metal-to-insulator transition*—is characterized by divergence of  $\xi$  according to,

$$\xi \propto |W - W_c|^{-\nu}, \quad (2)$$

where  $W_c$  is the critical value of the disorder intensity  $W$ . Both the scaling theory and other theoretical formulations of the problem of electron localization problem [10] predict that, the lower critical dimension  $d_c$  for electron localization (i.e., the spatial dimension *below* which all the electronic states are localized) is,  $d_c = 2$ . Over the years, extensive numerical simulations have also been carried out to confirm such predictions [11].

An important implication of the wave characteristics of electrons is that, the localization phenomenon may also occur in propagation of the *classical* waves in disordered media—acoustic and elastic waves. There is, however, a fundamental difference between the two problems. Electrons in a material interact with each other via long-ranged Coulomb interactions. Not only do such interactions play a fundamental role in the localization of the electronic states, but they also make the study of the problem in strongly heterogeneous materials very difficult [12–16]. On the other hand, classical waves, such as seismic waves, do not interact with one another and, therefore, it is their *scattering* in a heterogeneous medium that may cause their localization. As such, propagation of classical waves in such highly heterogeneous media as rock provides an ideal model for studying the localization phenomenon.

Localization of the classical waves in a heterogeneous medium has important practical implications. Consider, for example, a seismic experiment (typically carried out by creating an explosion on the ground) for, for example, exploring rock's structure and heterogeneity, represented by the spatial distributions of its elastic constants and the porosity, the anisotropy caused by stratification, and its fractures and faults. Such heterogeneities cause multiple scattering and interference of the waves. The question to be addressed is, can the heterogeneity and the associated scattering and interference effects give rise to localization of the waves? If the answer is affirmative, it would imply that useful information on rock's structure and properties can be

obtained only over distances  $r$  from the explosion's site that are at most of the order of the localization length  $\xi$  for the waves. In other words, if, for example,  $\xi$  is on the order of a few kilometers, but the linear size of an oil reservoir for which the seismic exploration is carried is larger than  $\xi$ , seismic recordings can provide only partial information for the reservoir.

As another example, consider the analysis of the seismic waves that are emanated from an earthquake hypocenter in rock. If the station that collects data for such waves is at a distance from the hypocenter which is larger than the localization length of the propagating seismic wave, no useful information can be gleaned from the data, as the data should represent essentially scattered noise.

Motivated by such fundamental questions and issues, our group has been studying propagation of both acoustic and elastic waves in strongly heterogeneous media. We have been investigating propagation of such waves in disordered media in which the heterogeneities, represented by the spatial distribution of the local elastic constants, are broadly distributed. We have considered both an uncorrelated distribution of the local elastic constants and also, consistent with the results of recent analysis of the data [5], a correlated distribution with a power-law, nondecaying correlation function. The aim of our study has been addressing the important question of whether acoustic and/or elastic waves can be localized in such disordered media.

We have been studying the problem by two different approaches. In one, we have developed a field-theoretic method to study the problem analytically. The approach is based on the method first introduced by Martin, Siggia, and Rose (MSR) [17] for analyzing dynamical critical phenomena. The method is an approximation, but has proven completely reliable for the study of disordered media. The second approach has been based on the numerical simulations of the governing equation for propagation of acoustic and elastic waves in disordered media. As described below, our study has shown that there is a *disorder-induced* transition from delocalized to localized waves in *any* spatial dimension  $d$ .

Theoretical studies of localization of acoustic waves were previously carried out by several groups [18–23]. For example, Baluni and Willemsen [23] studied propagation of acoustic waves in a 1D layered medium, composed of blocks of different elastic constants in series, and showed that the waves are localized. In addition, there have been several recent experimental studies of localization of waves in various disordered media [24–27]. However, the previous theoretical studies did not consider the problem in the type of strongly disordered media that we have been studying, nor did they study the problems in the context of the issues that are of interest to us. In addition, the dynamical renormalization group (RG) method that we utilize has not been used before for studying of propagation of classical waves in disordered media.

The rest of this paper is organized as follows. In Sect. 2 we present the summary of a MSR formulation for the propagation of acoustic waves in heterogeneous media. Also discussed are the physical implications of the RG results. The analytical results obtained by the RG method are tested in Sect. 3, where we describe the results of extensive numerical simulations. Section 4 is devoted to the description of a summary of the RG analysis of propagation of elastic waves in 2D disordered media, while numerical results that corroborate the RG analysis are described in Sect. 5. How to distinguish propagation of waves in disordered media with short-range correlations from those with long-range ones is described in Sect. 6. The most salient features of the results are summarized in Sect. 7, where we also describe briefly the relation between the shape of a wave front in heterogeneous media and the correlation function that characterizes the spatial distribution of the local elastic constants.

## 2 Renormalization group analysis of propagation of acoustic waves

To study acoustic wave propagation in a disordered medium with a spatial distribution of the local elastic constants, we analyze the scalar wave equation [1,28]:

$$\frac{\partial^2}{\partial t^2} \psi(\mathbf{x}, t) - \nabla \cdot [K(\mathbf{x}) \nabla \psi(\mathbf{x}, t)] = 0, \quad (3)$$

where  $\psi(\mathbf{x}, t)$  is the wave amplitude (a complex quantity) at time  $t$ , and  $K(\mathbf{x}) = e(\mathbf{x})/m$  the ratio of the elastic stiffness  $e(\mathbf{x})$  and the medium's mean density  $m$ . Equation (3) is valid in any spatial dimension  $d$  ( $d = 1, 2$ , and 3). Usually, propagation of the  $P$ -waves in an elastic medium is described by Eq. (3) [1,28], in which case  $K(\mathbf{x})$  represents (to which a constant factor  $m$ ) the bulk modulus, and hereafter will be referred as such. Real disordered (solid) materials support the propagation of both  $P$ - and  $S$ -waves. Propagation of elastic waves is described in Sects. 4 and 5.

To introduce the spatial distribution of  $K(\mathbf{x})$  and its correlation function into the analysis, we write  $K$  as,

$$K(\mathbf{x}) = K_0 + \eta(\mathbf{x}), \quad (4)$$

where  $K_0 = \langle K(\mathbf{x}) \rangle$ . Here,  $\eta(\mathbf{x})$  is assumed to be a Gaussian random process with a zero mean and the covariance,

$$\langle \eta(\mathbf{x})\eta(\mathbf{x}') \rangle = 2C(|\mathbf{x} - \mathbf{x}'|) = 2W_0\delta^d(\mathbf{x} - \mathbf{x}') + 2W_\rho|\mathbf{x} - \mathbf{x}'|^{2\rho-d}, \quad (5)$$

in which  $W_0$  and  $W_\rho$  represent, respectively, the intensity of the disorder due to the random (uncorrelated) and power-law correlated parts of the disorder. Note that we make no reference to the system's geometry. Its structure is represented only by the spatial distribution of the local elastic constants.

Consider a wave component with angular frequency  $\omega$  by taking the temporal Fourier transformation of  $\psi(\mathbf{x}, t)$  [29,30],

$$\psi(\mathbf{x}, \omega) = \frac{1}{(2\pi)^d} \int dt \exp(i\omega t) \psi(\mathbf{x}, t). \quad (6)$$

Equations (3) and (6) then yield the following for the propagation of a wave component with a frequency  $\omega$ :

$$f(\psi) = \nabla^2 \psi(\mathbf{x}, \omega) + \frac{w^2}{K_0} \psi(\mathbf{x}, \omega) + \nabla \cdot \left[ \frac{\eta(\mathbf{x})}{K_0} \nabla \psi(\mathbf{x}, \omega) \right] = 0. \quad (7)$$

The Gaussian nature of the noise  $\eta(\mathbf{x})$  leads us to write the following *generating functional* for the wave function:

$$\begin{aligned} P[\psi_R, \psi_I, \eta] &\sim \int D\eta D\psi_R D\psi_I \delta[f(\psi_R)] \delta[f(\psi_I)] J \left[ \frac{\partial f(\psi_R)}{\partial \psi_R} \right] J \left[ \frac{\partial f(\psi_I)}{\partial \psi_I} \right] \\ &\times \exp \left[ - \int d\mathbf{x} d\mathbf{x}' \eta(\mathbf{x}) D(\mathbf{x} - \mathbf{x}') \eta(\mathbf{x}') \right], \end{aligned} \quad (8)$$

where  $\psi_R(\mathbf{x})$  and  $\psi_I(\mathbf{x})$  are, respectively, the real and imaginary components of the wave function (both satisfying Eq. 3), and  $D(\mathbf{x} - \mathbf{x}')$  is the inverse of the correlation function  $C(\mathbf{x} - \mathbf{x}')$  that satisfies the following equation:

$$\int d\mathbf{x}'' C(\mathbf{x} - \mathbf{x}'') D(\mathbf{x}'' - \mathbf{x}') = \delta(\mathbf{x} - \mathbf{x}'). \quad (9)$$

In Eq. (8),  $J[\partial f(\psi_R)/\partial \psi_R]$  and  $J[\partial f(\psi_I)/\partial \psi_I]$  are the Jacobians given by

$$\begin{aligned} J &= \det \left\{ \frac{\partial f[\psi(\mathbf{x})]}{\partial \psi(\mathbf{x}')} \right\} \\ &= \det \left\{ \nabla^2 \delta(\mathbf{x} - \mathbf{x}') + \frac{w^2}{K_0} \delta(\mathbf{x} - \mathbf{x}') + \nabla \cdot \left[ \frac{\eta(\mathbf{x})}{K_0} \nabla \delta(\mathbf{x} - \mathbf{x}') \right] \right\}. \end{aligned} \quad (10)$$

Using the MSR method [17], one writes the delta function as a Gaussian integral over *auxiliary* fields  $\tilde{\psi}_R(\mathbf{x})$  and  $\tilde{\psi}_I(\mathbf{x})$  [29,30]. On the other hand, using the integral representation of the determinant by the anti-commuting variables, we can also write the Jacobian as a Gaussian integral over fields  $\chi$  and  $\chi^*$  that are called *Grassmanian* (where \* indicates a complex-conjugate property). Therefore, Eq. (8) is rewritten as

$$P[\psi, \psi, \chi, \chi^*, \eta] \sim \int [D\psi][D\tilde{\psi}][D\chi][D\chi^*][D\eta] \exp[-S(\psi, \tilde{\psi}, \chi, \chi^*, \eta)], \quad (11)$$

where the *action*  $S(\psi, \tilde{\psi}, \chi, \chi^*, \eta)$  is given by

$$\begin{aligned}
S = & \int d\mathbf{x}d\mathbf{x}' \left[ i\tilde{\psi}_R(\mathbf{x}') \left( \nabla^2 + \frac{w^2}{K_0} \right) \psi_R(\mathbf{x}) + i\tilde{\psi}_I(\mathbf{x}') \left( \nabla^2 + \frac{w^2}{K_0} \right) \psi_I(\mathbf{x}) \right. \\
& - i\frac{\eta}{K_0}(\mathbf{x}) \nabla \tilde{\psi}_R(\mathbf{x}') \nabla \psi_R(\mathbf{x}) - i\frac{\eta}{K_0}(\mathbf{x}) \nabla \tilde{\psi}_I(\mathbf{x}') \nabla \psi_I(\mathbf{x}) \\
& + \chi_R^*(\mathbf{x}') \left( \nabla^2 + \frac{w^2}{K_0} \right) \chi_R(\mathbf{x}) + \chi_I^*(\mathbf{x}') \left( \nabla^2 + \frac{w^2}{K_0} \right) \chi_I(\mathbf{x}) \\
& \left. - \frac{\eta}{K_0}(\mathbf{x}) \nabla \chi_R^*(\mathbf{x}') \nabla \chi_R(\mathbf{x}) - \frac{\eta}{K_0}(\mathbf{x}) \nabla \chi_I^*(\mathbf{x}') \nabla \chi_I(\mathbf{x}) \right] \delta(\mathbf{x} - \mathbf{x}') \\
& - \eta(\mathbf{x}) D(\mathbf{x} - \mathbf{x}') \eta(\mathbf{x}').
\end{aligned} \tag{12}$$

Using Gaussian integration we integrate  $\eta$  out in Eq. (11). That is, we integrate over the local disorder in order to generate a coarser system at larger length scales, which is the key idea in any RG analysis. This procedure generates an *effective action*  $S_e$  at a coarser scale, with

$$P[\psi, \psi, \chi, \chi^*] \sim \int [D\psi][D\tilde{\psi}][D\chi][D\chi^*] \exp\{-S_e[\psi, \tilde{\psi}, \chi, \chi^*]\}. \tag{13}$$

where  $S_e$ , the effective action which describes the medium at the coarser scale, is given by,

$$\begin{aligned}
S_e = & \int d\mathbf{x}d\mathbf{x}' \left[ \left( i\tilde{\psi}_I(\mathbf{x}') \left( \nabla^2 + \frac{\omega^2}{K_0} \right) \psi_I(\mathbf{x}) + i\tilde{\psi}_R(\mathbf{x}') \left( \nabla^2 + \frac{\omega^2}{K_0} \right) \psi_R(\mathbf{x}) \right) \delta(\mathbf{x} - \mathbf{x}') \right] \\
& + (\chi_I^*(\mathbf{x}') \left( \nabla^2 + \frac{\omega^2}{K_0} \right) \chi_I(\mathbf{x}) + \chi_R^*(\mathbf{x}') \left( \nabla^2 + \frac{\omega^2}{K_0} \right) \chi_R(\mathbf{x})) \delta(\mathbf{x} - \mathbf{x}') \\
& + \left( i\nabla \tilde{\psi}_I \nabla \psi_I + i\nabla \tilde{\psi}_R \nabla \psi_R + \nabla \chi_I^* \nabla \chi_I + \nabla \chi_R^* \nabla \chi_R \right) \frac{C(\mathbf{x} - \mathbf{x}')}{K_0^2} \\
& \times \left( i\nabla \tilde{\psi}_I \nabla \psi_I + i\nabla \tilde{\psi}_R \nabla \psi_R + \nabla \chi_I^* \nabla \chi_I + \nabla \chi_R^* \nabla \chi_R \right) \Big].
\end{aligned} \tag{14}$$

Two coupling constants,  $g_0 = W_0/K_0^2$ , and,  $g_\rho = W_\rho/K_0^2$ , appear in  $S_e$ , when we substitute Eq. (5) for the function  $C(\mathbf{x} - \mathbf{x}')$  into Eq. (14).

The key properties to be determined by such a RG analysis in the *critical limit*, i.e., when  $\omega^2/K_0 \rightarrow 0$ , are the so-called  $\beta$ -functions. But, the analysis is perturbative in that, the  $\beta$ -function can be determined to various orders—or *loops* as they are called in the RG analyses. As the above analysis indicates, determining the  $\beta$ -functions, even to one-loop order, is a complex task. The  $\beta$ -functions are derived from the effective action  $S_e$  which, as described above, is obtained by integrating the generating functional  $P$  over the local disorder. Without getting into the mathematical details of the procedure, the following steps are taken in order to derive the  $\beta$ -functions.

- (1) As described above, we work with the Fourier representation of effective action  $S_e$ , i.e., in the momentum space. We must, therefore, introduce a momentum cutoff  $\Lambda$ , the existence of which due to a nonzero lattice constant for any disordered material.
- (2) The momentum space is then divided into two regions:  $k \geq (\Lambda)/l$  (region 1, fast modes), and  $k < (\Lambda)/l$  (slow modes), where  $k$  is the momentum (mode), and  $l$  a rescaling factor which is somewhat larger than one, i.e.,  $l = 1 + \delta_l$  ( $\delta_l \ll 1$ ). Then, in the generating functional which has an integration over all the fields with any momentum, we integrate over the fast modes, i.e., over those fields with momenta in region 1.
- (3) We then rewrite the resulting generating functional in the original form, by redefining the couplings in the effective action  $S_e$ . By coupling we mean the coefficients of the different terms in the action. We use the fact that

$$\langle \exp(S_e) \rangle = \exp \left[ \langle S_e \rangle + \frac{1}{2!} (\langle S_e^2 \rangle - \langle S_e \rangle^2) + \dots \right].$$

Some of the terms that appear in the effective action at the coarser scale are similar to those in the action for the finer scale, but with different numerical coefficients. Some new terms may also emerge as a result

- of rescaling, but can be shown to be irrelevant. There are also terms both in the first- and second-order terms in the above expansion that are divergent. However, all the divergent terms cancel each other out.
- (4) A further rearrangement of the terms is necessary, in order to make the volume of rescaled momentum space to be equal to the original one. This is done easily by rescaling any variable  $\zeta$  in the momentum space to  $l\zeta$ .
  - (5) The above steps generate new couplings  $g'_i$  ( $i = 1$  and  $2$ ) as functions of the old ones, and the scale parameter  $l$ , i.e.,  $g'_i = \mathcal{R}_i(g_1, g_2, l)$ . The  $\beta$ -functions are then given by

$$\beta_i = \frac{\partial g'_i}{\partial \ln l}.$$

Any RG analysis is facilitated by using diagrammatic representation of the relevant terms that appear in the perturbative evaluation of the effective action. These are the so-called Feynman diagrams, each one of which represents the corrections (in the perturbation analysis) to the various terms. The higher the loop order, the larger is the number of such Feynman diagrams. For example, in the one-loop order that we develop here, there are nine distinct Feynman diagrams that contribute to the correction to the four-point correlation function  $\langle \psi_R(\mathbf{x}_1) \tilde{\psi}_R(\mathbf{x}_2) \psi_R(\mathbf{x}_3) \tilde{\psi}_R(\mathbf{x}_4) \rangle$ . The complete details are given elsewhere [30]. It can then be shown that, under a change of scale from  $\mathbf{x}$  to  $l\mathbf{x}$  the dimensions of the coupling parameters are given by

$$[g_0] = d, \quad (15)$$

$$[g_\rho] = d - 2\rho. \quad (16)$$

The  $\beta$ -functions,  $\beta(\tilde{g}_0)$  and  $\beta(\tilde{g}_\rho)$ , are then given by [29,30]

$$\beta(\tilde{g}_0) = \frac{\partial \tilde{g}_0}{\partial \ln l} = -d\tilde{g}_0 + 8\tilde{g}_0^2 + 10\tilde{g}_\rho^2 + 20\tilde{g}_0\tilde{g}_\rho, \quad (17)$$

$$\beta(\tilde{g}_\rho) = \frac{\partial \tilde{g}_\rho}{\partial \ln l} = (2\rho - d)\tilde{g}_\rho + 12\tilde{g}_0\tilde{g}_\rho + 16\tilde{g}_\rho^2, \quad (18)$$

where

$$\tilde{g}_0 = k_d \left[ \frac{d+5}{2d(d+2)} \right] g_0, \quad (19)$$

$$\tilde{g}_\rho = k_d \left[ \frac{d+5}{2d(d+2)} \right] g_\rho, \quad (20)$$

with  $k_d = S_d/(2\pi^d)$ , and  $S_d$  being the surface area of the  $d$ -dimensional unit sphere.

For certain values of the couplings the  $\beta$ -functions vanish. Such roots of the  $\beta$ -functions are the *fixed points* (FPs) of the RG transformation, i.e., those that remain invariant under the transformation. That is, they remain invariant as one sums over the short-wavelength degrees of freedom—i.e., integrates over local disorder—in order to generate a coarser medium at a larger length scale. Since the FPs remain invariant under the RG transformation, they determine how disorder affects wave propagation as one passes from the fine to coarser scales.

The  $\beta$ -functions describe the RG flow diagrams in the space of the couplings of the action. If a matrix  $\mathbf{M}$  is defined by  $M_{ij} = \partial\beta_i/\partial g_j$ , with the derivatives evaluated at the FPs, then the eigenvectors of  $\mathbf{M}$  define the *eigendirections* of the RG transformation. The eigenvectors define a new coordinate system in the vicinity of the FPs. The sign of an eigenvalue corresponding to any eigenvector also fixes the direction of the RG flow. If the eigenvalue is positive, the RG flow along the corresponding eigendirection moves away from the FP. Conversely, if the eigenvalue is negative, the RG flow along the corresponding eigendirection moves towards the FP, in which case the FP is called an *attractive* fixed point.

As already mentioned, the  $\beta$ -functions describe how the two couplings— $g_0$  and  $g_\rho$ —evolve if we rescale all the lengths and consider the elastic medium at coarser scales. If we find, for example, that a small  $g_0$  diverges under the RG rescaling, it implies that a small  $g_0$  at small length scales behaves like a very strong disorder at much larger scales. The implications would then be that the disorder is *relevant* and, therefore, every wave amplitude will be localized. If, on the other hand, we find, for example, that for some  $g_0 < g_c$  (where  $g_c$  is a critical value)  $g_0$  vanishes under the RG rescaling, it will imply that in this regime  $g_0$  does not contribute much to the behavior of the propagating waves at large length scales. Therefore, a localized state may be defined as follows: we have localized states if, under the RG rescaling, *at least* either  $g_0$  or  $g_\rho$  diverges.

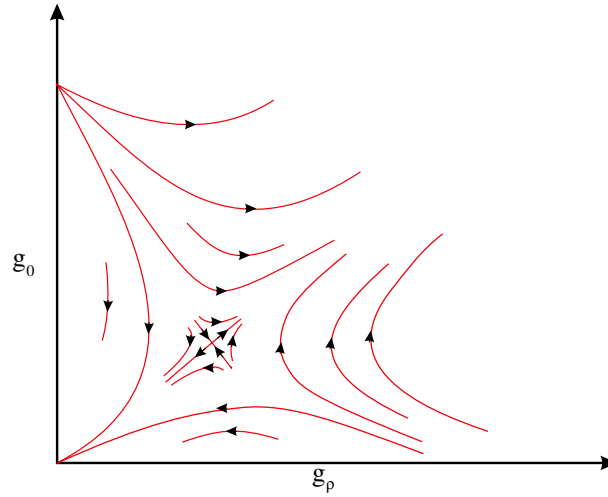


**Fig. 1** Flows in the coupling constants space for  $0 < \rho < \frac{1}{2}d$

In order to understand the predictions of the RG analysis, one must examine the RG flows, Eqs. (20) and (21). They reveal that, depending on  $\rho$  (the parameter that characterizes the correlation function of the power-law correlated disorder), there can be two distinct regimes [29,30]:

- (i) For  $0 < \rho < \frac{1}{2}d$  there are three sets of FPs: The trivial set representing the Gaussian FPs,  $g_0^* = g_\rho^* = 0$ , which is *stable*, and two other sets representing nontrivial FPs and the corresponding *eigendirections*. One is  $\{g_0^* = \frac{1}{8}d, g_\rho^* = 0\}$ , while the other set is given by

$$g_0^* = -\frac{4}{21} \left[ d + \frac{5}{16}(2\rho - d) \right] + \frac{4}{21} \sqrt{\left[ d + \frac{5}{16}(2\rho - d) \right]^2 + \frac{55}{256}(2\rho - d)^2},$$

$$g_\rho^* = -\frac{3}{4}g_0^* + \frac{1}{16}(d - 2\rho),$$
(21)

which is stable in one eigendirection but unstable in the other eigendirection. The corresponding RG flow diagram is shown in Fig. 1. Therefore, for  $0 < \rho < \frac{1}{2}d$  the one-loop RG analysis indicates that a medium with *uncorrelated* disorder is *unstable* against long-range correlated disorder towards a *new* FP in the space of the coupling constants. This means that there is a *phase transition* from delocalized to localized states with increasing the disorder intensity.

Thus, the physical implication of the RG results becomes clear. Figure 1 indicates that, in the interval  $0 < \rho < \frac{1}{2}d$ , there is a region in the space of the coupling constants  $\{g_0, g_\rho\}$  in which the RG flows take any initial point to the Gaussian FP,  $\{g_0 = g_\rho = 0\}$ . Physically, this implies that in this region a disordered medium of the type considered in this paper looks like a pure (non-disordered or homogeneous) medium at large length scales, implying that the waves are *extended* or delocalized.

However, when  $g_0$  or  $g_\rho$  are large enough that the initial point is out of the basin of attraction of the Gaussian FP, the RG flow moves such points towards large values, hence implying that, under the RG rescaling, the probability density function of the disorder becomes *broader* at larger and larger length scales. Therefore, in this case, a propagating wave samples a medium with very large spatial fluctuations in the elastic moduli. Moreover, note that even if one starts in a disordered medium with purely long-range correlations (i.e., one with  $g_0 = 0$ ), one finds from the RG equations that the growth of  $g_\rho$  will lead to increasing, i.e., *nonzero*,  $g_0$ , hence implying that *uncorrelated* disorder will be produced by the RG rescaling. Since the local fluctuations in the bulk moduli (and, more generally, the local stiffness) play the role of scattering points, the implication is that multiple scattering of a propagating wave from the uncorrelated disorder will destroy the wave's coherence, leading eventually to its localization. This is the basis of the localization-delocalization transition in the low-frequency limit, in terms of the disorder intensity.

- (ii) For  $\rho > \frac{1}{2}d$  there are two FPs: the Gaussian FP which is stable on the  $g_0$  axis but not on the  $g_\rho$  axis, and the nontrivial FP,  $\{g_0^* = \frac{1}{8}d, g_\rho^* = 0\}$ , which is unstable in all directions. The corresponding RG flow

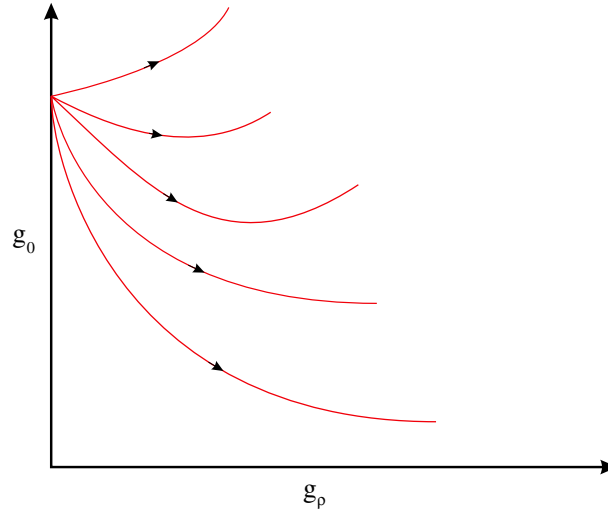


**Fig. 2** Flows in the coupling constants space for  $\rho > \frac{1}{2}d$

diagram is shown in Fig. 2. The implication is that, although power-law correlated disorder is *relevant*, no new FP exists to one-loop order and, therefore, the system's long-wavelength behavior is determined by the long-range component of the disorder. Physically this means that for  $\rho > \frac{1}{2}d$ , the waves are localized for *any*  $d$ . In addition, in both cases the system undergoes a *disorder-induced* transition when only the uncorrelated disorder is present.

Let us mention that the above results are general as long as  $W_\rho > 0$  (which is the only physically acceptable limit). For  $W_\rho < 0$  the above phase space is valid for  $\rho > \frac{1}{2}(d + 1)$ .

We also point out that it is convenient to begin the RG rescaling and analysis with the assumption that the couplings  $g_0$  and  $g_\rho$  are small. If, under the RG rescaling, we find stable FPs, it would imply that the assumption of the couplings being small about such a FP is valid. Around the unstable FP, however, the couplings can grow and, hence, the perturbation analysis that we have developed would fail. But, for our purpose, i.e., to determine the localized/extended regimes, the most important goal is to determine the condition(s) under which the FPs are unstable, so that the couplings can diverge.

### 3 Numerical simulation of acoustic wave propagation

Are the RG predictions confirmed by numerical simulations? We have carried out extensive numerical simulations of the problem in 1D, 2D and 3D systems [29–32]. We do not describe the results for 1D media; they are given elsewhere [32]. Instead, a few key results of the numerical simulations of acoustic wave propagation in disordered 2D and 3D media are described here.

To carry out numerical simulations of Eq. (3) in 2D and 3D media, we used the finite-difference (FD) method with second-order discretization for the time and fourth-order discretization for the spatial variables. Consider, for example, the 2D media. In discretized form,  $\psi(\mathbf{x}, t)$  is written as  $\psi_{i,j}^{(n)}$ , where  $n$  denotes the time step number. The second-order FD approximation (accurate to  $\Delta t^2$ ) to the time-dependent term of Eq. (3) is the standard form,

$$\partial^2 \psi(\mathbf{x}, t) / \partial t^2 \simeq \frac{1}{\Delta t^2} \left( \psi_{i,j}^{(n+1)} - \psi_{i,j}^{(n)} + \psi_{i,j}^{(n-1)} \right), \quad (22)$$

where  $\Delta t$  is the time step's size. As for the spatial derivatives, we first expand the right side of Eq. (3) as

$$\begin{aligned} \nabla \cdot [K(\mathbf{x}) \nabla \psi(\mathbf{x}, t)] &= \nabla K(\mathbf{x}) \cdot \nabla \psi(\mathbf{x}, t) + K(\mathbf{x}) \nabla^2 \psi(\mathbf{x}, t) \\ &= \partial_x K(\mathbf{x}) \partial_x \psi(\mathbf{x}, t) + \partial_y K(\mathbf{x}) \partial_y \psi(\mathbf{x}, t) \\ &\quad + K(\mathbf{x}) \left[ \partial_x^2 \psi(\mathbf{x}, t) + \partial_y^2 \psi(\mathbf{x}, t) \right]. \end{aligned}$$

Then, using the fourth-order FD discretization, we obtain for, for example, the derivatives in the  $x$ -direction,

$$\partial_x^2 \psi(\mathbf{x}, t) \simeq \frac{-\psi_{i+2,j}^{(n)} + 16\psi_{i+1,j}^{(n)} - 30\psi_{i,j}^{(n)} + 16\psi_{i-1,j}^{(n)} - \psi_{i-2,j}^{(n)}}{12\Delta x^2}, \quad (23)$$

and

$$\partial_x \psi(\mathbf{x}, t) \simeq \frac{-\psi_{i+2,j}^{(n)} + 8\psi_{i+1,j}^{(n)} - 8\psi_{i-1,j}^{(n)} + \psi_{i-2,j}^{(n)}}{12\Delta x}, \quad (24)$$

where  $\Delta x$  is the spacing between two neighboring grid points in the  $x$ -direction. Similar expressions are written down for the partial derivatives with respect to the  $y$ -direction (and the  $z$ -direction for the simulations in 3D). Such approximations proved to be accurate enough and provided the required stability to the numerical results, as we work in the limit of low frequencies or long wavelengths [33]. We used  $L_x \times L_y$  grids in 2D with  $L_x = 8,000$  and  $L_y = 400$  (where  $x$  is the main direction of wave propagation), and  $L_x \times L_y \times L_z$  grids in 3D with  $L_x = L_y = 70$ , and  $L_z = 500$  (where  $z$  is the main direction of wave propagation). The parameter  $K(\mathbf{x})$ , representing the gridblock-scale bulk modulus, was distributed spatially with the power-law correlation function described above.

Two distinct classes of disordered media were considered. In one case, the disordered media studied were isotropic. In this case the spatial distribution of  $K(\mathbf{x})$  was generated using the midpoint displacement method [34] (we took  $W_\rho = 1.0$ ). In the second case, the media studied were anisotropic. While one may consider a variety of anisotropic media, we considered, consistent with the structure of rock [3,4], the anisotropy that is caused by stratification. Such disordered media contain layers with sharp contrasts between them. To generate the spatial distribution of the local bulk moduli in the layered media, we used a fast Fourier transformation technique [35–37]. Note that  $H = \rho - 1$  is the Hurst exponent with  $0 \leq H \leq 1$ , such that  $H > 1/2$  ( $< 1/2$ ) implies positive (negative) correlations in the increments of the values generated by the distribution, whereas  $H = 1/2$  is the usual Brownian (uncorrelated) case. We also carried out simulations for the case in which values of  $K(\mathbf{x})$  were uncorrelated and uniformly distributed, but with the same variance as that of the power-law case.

To begin the simulations, a pulse wave source located at every node of the first row of the grid at  $y = 0$  (in 2D), or at every node of the  $xy$  plane at  $z = 0$  (in 3D), was used. Such a boundary condition ensured generation of a smooth initial wave front. As the source function  $S(t)$  we used the following to generate the pulse waves (any other source may be used):

$$S(t) = -A(t - t_0) \exp[-\zeta(t - t_0)^2], \quad (25)$$

where  $A$  is a constant and  $\zeta$  controls the wave's wavelength. The discretized wave equation was then solved numerically throughout the system. Periodic boundary conditions were imposed in the lateral direction(s), which did not distort the nature of the wave propagation, as we used large system sizes. The discretized equations were integrated with up to 96,000 time steps in 2D and 24,000 time steps in 3D. The accuracy of the solution was checked by considering the stability criterion and the wavelength of the source [32]. To compute the amplitude decay in the medium, we collected the numerical results for the wave's amplitude at 80 receivers (grid points), distributed evenly throughout the grid, along the main direction of wave propagation. The results were averaged over 45 realizations of the system.

Figure 3 presents the decay in the wave amplitude through a uniformly random 2D medium, and that of a 2D anisotropic medium with a nondecaying power-law correlation function for the local bulk modulus  $K(\mathbf{x})$ , with  $\rho = 1.2$  and  $1.5$ . The wave amplitudes for the correlated cases decline very rapidly, much faster than those in the uniformly random medium. The results shown in Fig. 3 are consistent with the RG prediction that acoustic waves in 2D systems must be localized for  $\rho > \frac{1}{2}d = 1$ .

To see the differences between propagation of acoustic waves and electron localization, we recall that in the latter case, the amplitudes  $\psi(\mathbf{x})$  in *isotropic* media decay according to Eq. (1). However, it is not yet clear how  $\psi$  decays in an *anisotropic medium* of the type that we have been studying. The amplitude decay in such anisotropic media should presumably depend on whether the main direction of wave propagation is (more or less) parallel to the strata or perpendicular to them. Therefore, we rewrite Eq. (1) in a slightly more general form,

$$\psi(\mathbf{x}) = \psi_0 \exp[-(|\mathbf{x}|/\xi)^\gamma]. \quad (26)$$

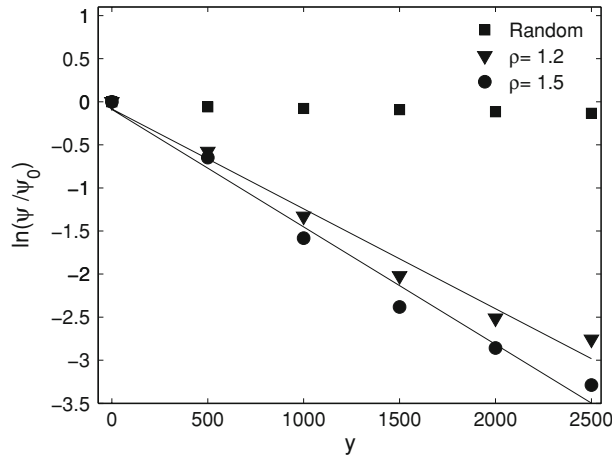


**Fig. 3** Wave amplitudes in 2D anisotropic media, for random and power-law correlated bulk moduli. The main direction of wave propagation is parallel to the strata. The *straight lines* indicate exponential decay of the amplitude

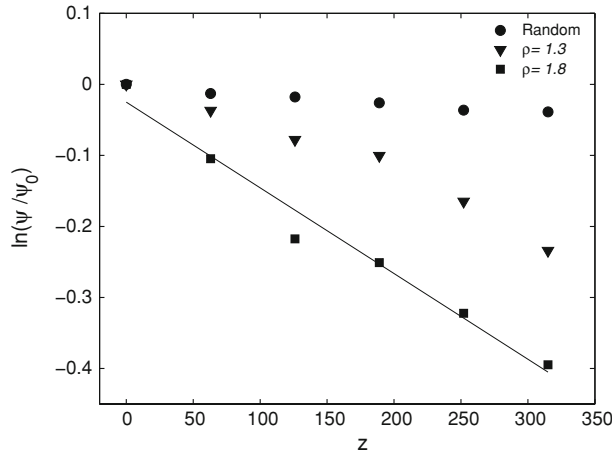


**Fig. 4** Wave amplitudes in 3D isotropic media with negative ( $\rho = 1.3$ ) and positive ( $\rho = 1.8$ ) correlations, and their comparison with uncorrelated media. The RG analysis indicates that for  $\rho > 1.5$  the waves must be localized and, therefore, their amplitudes must decay exponentially. The *straight line* indicates that this is the case

If we fit the results for the 2D correlated media shown in Fig. 3 to Eq. (1) (which are for the case in which the main direction of wave propagation is parallel to the strata), we find that  $\gamma \simeq 1$  for both values of  $\rho$ . That is, one has the usual localization in which the wave's amplitude decays exponentially with the distance from the source.

Figure 4 presents the decay of the waves' amplitude in isotropic 3D media for  $\rho = 1.3$  (negative correlations) and  $\rho = 1.8$  (positive correlations). Also shown are the results for a uniformly random 3D medium, but with the same variance as that of the correlated distribution of the local bulk moduli. When the correlations are positive ( $\rho = 1.8$ ), the decay in the wave amplitudes is essentially exponential (indicated by the straight line), because there are zones of positively correlated (more or less similar) elastic constants that help to trap the wave front, hence resulting in the rapid decay of the amplitudes. A fit of the numerical results for  $\rho = 1.8$  to Eq. (26) also confirms that  $\gamma \simeq 1$ , consistent with the RG prediction that, in 3D, for  $\rho > \frac{1}{2}d = 3/2$  the waves must be localized. In contrast, the wave amplitudes in the random medium are practically constant, while in the medium with  $\rho = 1.3 < 3/2$  the amplitudes do not seem to decay rapidly enough. While the RG analysis does not predict localization of the waves in 3D systems with  $\rho < 1.5$ , a fit of the results for  $\rho = 1.3$  shown in Fig. 4 indicates that  $\gamma \simeq 0.1$ , although this estimate of  $\gamma$  is not very accurate because the computational grid is somewhat short.

#### 4 Renormalization group analysis of propagation of elastic waves

The same type of RG analysis can also be used for studying propagation of elastic waves in disordered media [38]. The equation of motion for an elastic medium with the mean density  $m$  is given by

$$m \frac{\partial^2 u_i}{\partial t^2} = \partial_j \sigma_{ij}, \quad (27)$$

where  $u_i$  is the displacement in the  $i$ th direction, and  $\sigma_{ij}$  the  $ij$ th component of the stress tensor  $\sigma$ . As usual,  $\sigma_{ij}$  is expressed in terms of the strain tensor,

$$\sigma_{ij}(\mathbf{x}) = 2\mu(\mathbf{x})u_{ij} + \lambda(\mathbf{x})u_{kk}\delta_{ij}, \quad (28)$$

while for small deformations, the strain tensor  $\mathbf{u}$  is given by

$$u_{ij} = \frac{1}{2}(\partial_i u_j + \partial_j u_i), \quad (29)$$

where  $\lambda$  and  $\mu$  are usual the Lamé coefficients. For simplicity, we take the two Lamé coefficients to be equal, but the main results of the analysis will not change if they are unequal, but follow the same type of statistical distributions. Hence, we write

$$\mu(\mathbf{x}) = \lambda(\mathbf{x}) = \lambda_0 + \eta(\mathbf{x}), \quad (30)$$

where  $\lambda_0 = \langle \lambda(\mathbf{x}) \rangle$ , with  $\langle \cdot \rangle$  representing a spatial averaging. We assume that  $\eta(\mathbf{x})$ , the fluctuating part of the Lamé coefficients, is a Gaussian random process. Thus, in performing the spatial average over the disorder we use a probability distribution of the form

$$P[\eta(\mathbf{x})] \propto \exp \left[ - \int d\mathbf{x} d\mathbf{x}' \eta(\mathbf{x}) D(\mathbf{x} - \mathbf{x}') \eta(\mathbf{x}') \right], \quad (31)$$

where, as before,  $D(\mathbf{x})$  is the inverse of the correlation function  $C(\mathbf{x})$ . Similar to the case of acoustic waves, the disorder that we consider consists of two parts. One is random (uncorrelated), while the second part is characterized by a power-law correlation function. Hence, the overall correlation function of the spatial distribution of the disorder is given again by Eq. (5).

A Gaussian distribution of the form (31) gives rise to quadratic couplings in the interaction part of the action defined below. Moreover, it may include a tail of inadmissible negative values of the Lamé coefficients. In principle, the unphysical tail can be removed by introducing a modified probability distribution function which would, however, produce couplings of higher order in the action. But, interactions of orders higher than quadratic are irrelevant in the RG analysis and, therefore, can be ignored.

The RG analysis has been carried out for a 2D disordered elastic medium [38]. As in the case of the acoustic waves, we take the Fourier transform of Eq. (27) with respect to the time variable, which yields the governing equation for a monochromatic wave with angular frequency  $\omega$ ,

$$\partial_j \sigma_{ij} + \omega^2 m u_i \equiv \lambda_0 \mathcal{L}_{ij} u_j = 0. \quad (32)$$

Here,  $\mathcal{L}$  is a  $2 \times 2$  differential matrix operator. The RG analysis follows a path similar to what was described above for acoustic waves, except that, because we deal with the vector wave equation, the analysis, even for 2D media, is very involved. One obtains an MSR generating functional that corresponds to the (Fourier-transformed) wave equation. Then, integrating out the disorder function  $\eta$  by performing a Gaussian integration leads to an effective MSR action  $S_e$ , to which the RG analysis is applied. The analysis is complex and lengthy. After considerable mathematic analysis one obtains [37] the two key functions, namely, the two  $\beta$ -functions to one-loop order which, for 2D disordered media, are given by

$$\beta(\tilde{g}_0) \equiv \frac{\partial \tilde{g}_0}{\partial \ln l} = -2\tilde{g}_0 + \left(36 + \frac{937}{18}\right) \tilde{g}_0^2 + \frac{716}{27} \tilde{g}_\rho^2 + \left(36 + \frac{3635}{54}\right) \tilde{g}_0 \tilde{g}_\rho, \quad (33)$$

$$\beta(\tilde{g}_\rho) \equiv \frac{\partial \tilde{g}_\rho}{\partial \ln l} = (2\rho - 2)\tilde{g}_\rho + 72\tilde{g}_0 \tilde{g}_\rho + \left(36 + \frac{1948}{27}\right) \tilde{g}_\rho^2, \quad (34)$$

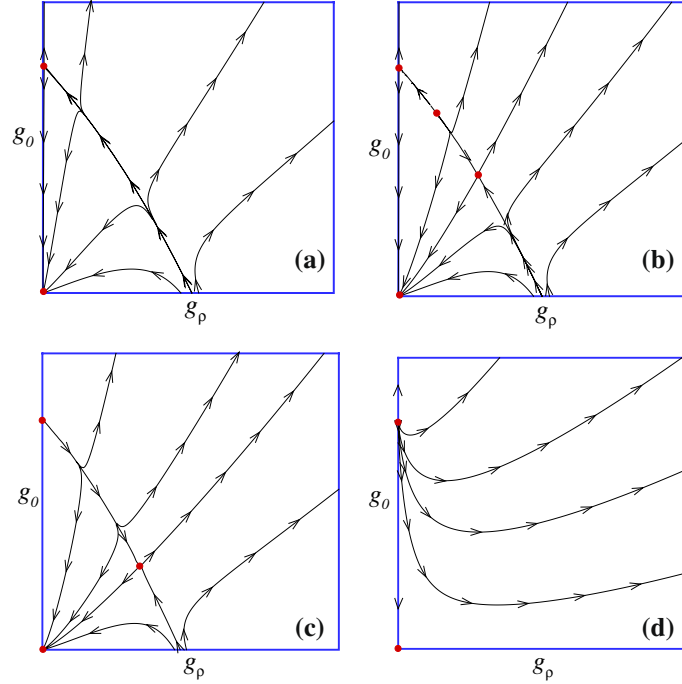


**Fig. 5** Renormalization group flows for **a**  $\rho < 0.14$ , **b**  $0.14 < \rho < 0.18$ , **c**  $0.18 < \rho < 1$ , and **d**  $\rho > 1$

where  $\tilde{g}_0$  and  $\tilde{g}_\rho$  are dimensionless coupling constants. Equations (33) and (34) should be compared with Eqs. (17) and (18) for the acoustic waves. The extension of the RG analysis to 3D systems is very complex, but doable.

The two  $\beta$ -functions describe how the two couplings— $g_0$  and  $g_\rho$ —evolve if we rescale all the lengths and consider the elastic medium at coarser scales. If, for example, a small  $g_0$  diverges under the RG rescaling, its physical implication is that a small  $g_0$  at small length scales behaves as very strong disorder at much larger scales. Therefore, under such a condition, every wave amplitude will be localized. If, on the other hand, for some  $g_0 < g_c$  (where  $g_c$  is a critical value)  $g_0$  vanishes under the RG rescaling, it implies that, in this regime,  $g_0$  does not contribute much to the evolution of the propagating waves at large length scales. Therefore, we define a localized state in the same way that we did for the acoustic waves, namely, the waves are localized if, under the RG rescaling, *at least* either  $g_0$  or  $g_\rho$  diverges.

As usual, the FPs of the RG transformation are the roots of  $\beta$ -functions. The RG equations, together with the disorder parameter  $\rho$ , have a complex phase space. Depending on  $\rho$ , there are four regimes:

(i) For

$$\rho < \frac{1}{3,888,601} \left( -17,557,527 + 128\sqrt{19,977,620,601} \right) \simeq 0.14,$$

there are two FPs: the trivial Gaussian FP,  $\{\tilde{g}_0^* = \tilde{g}_\rho^* = 0\}$ , which is stable, and a nontrivial FP,  $\{\tilde{g}_0^* = 36/1,585 \simeq 0.022, \tilde{g}_\rho^* = 0\}$  which has one positive eigenvalue (along the eigendirection of which is unstable) and one negative one (along the eigendirection of which is stable); see Fig. 5a. Physically, this implies that the RG flow diagram is divided into two parts. In one part the Gaussian FP is relevant and the disorder does not have any effect, so that all the states are delocalized. In the second part, the values of couplings increase under rescaling, so that the disorder (both uncorrelated and correlated) is relevant and, therefore, the elastic waves are localized. Thus, the curve that separates the two parts is where the localization-delocalization transition takes place.

(ii) Four FPs exist if  $0.14 < \rho < 289/1,585 \simeq 0.18$ . The Gaussian FP is stable. The other FPs are unstable in one eigendirection, but stable in the other eigendirection, except for  $\{\tilde{g}_0^* = 0.022, \tilde{g}_\rho^* = 0\}$ , which has positive eigenvalues and, hence, is unstable in *all* directions. This is shown in Fig. 5b.

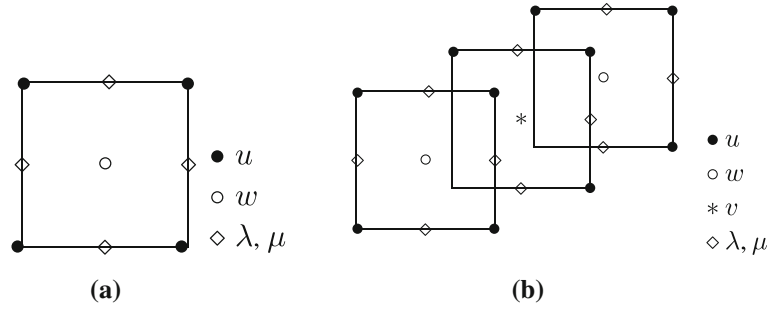


**Fig. 6** **a** Two- and **b** three-dimensional staggered grids used in the simulations. *Symbols* indicate the grid points at which the associated quantities are evaluated

- (iii) There are three FPs for  $0.18 < \rho < 1$ . The Gaussian FP is again stable. The FP  $\{g_0^* = 0.022, g_\rho^* = 0\}$  is unstable in all directions. The third FP is stable in one eigendirection but unstable in the second eigendirection. Figure 5c presents this part of the RG flow diagram.

In both (ii) and (iii), as  $\rho$  increases, the disordered medium tries to move away from case (i) (the delocalized-localized transition) to a purely localized state (see also below). Moreover, in (i)–(iii) there is a point on the  $g_\rho$  axis which obviously is *not* a FP, but the RG flows change their direction on the  $g_\rho$  axis at that point. This means that one of the  $\beta$ -functions is zero on this axis, while the other one is not.

- (iv) For  $\rho > 1$  there are two FPs. As Fig. 5d indicates, the Gaussian FP is stable on the  $\tilde{g}_0$  axis but unstable on the  $\tilde{g}_\rho$  axis, and the nontrivial FP,  $\{\tilde{g}_0^* = 0.022, \tilde{g}_\rho^* = 0\}$ , is unstable in all directions. The implication is that, while the power-law correlated disorder is relevant, no new FP exists to one-loop order and, therefore, the long-wavelength behavior of the system is determined by the long-range component of the disorder. This means that for  $\rho > 1$  the elastic waves are localized in 2D.

## 5 Numerical simulations of propagation of elastic waves

In the computer simulations [39] we took the Lamé coefficients  $\lambda$  and  $\mu$  to be uniformly distributed in the intervals  $[\lambda_0 - W_\lambda, \lambda_0 + W_\lambda]$  and  $[\mu_0 - W_\mu, \mu_0 + W_\mu]$ , where  $\lambda_0$  and  $\mu_0$  are the mean values of the coefficients. Accurate numerical simulation of Eq. (27) (together with Eqs. (28) and (29)) is difficult, and particularly so when one solves it for a heterogeneous medium in which the Lamé coefficients vary spatially. There have been many attempts in the geophysics literature to solve Eq. (1) numerically in the time domain, using a variety of schemes and computational grids [40]. Typically, in such works, Eq. (27) was discretized by the FD technique. However, use of the central-difference FD method, together with cubic computational grids, can give rise to certain instabilities in the solution. It has been shown [40] that stable numerical solutions are obtained if one uses a staggered computational grid, in order to define the variables and discretize Eq. (27), unless the medium contains singularities (such as cracks) or free surfaces, in which case a rotated staggered grid may be more appropriate.

In the present study we used the staggered computational grids shown in Fig. 6. Discretizing Eq. (27) on such a grid leads to a symmetric Hamiltonian, as expected. We then seek monochromatic solutions of Eq. (27) for a given frequency, in the form  $u_i(\mathbf{x}, t) = u_i(\mathbf{x}) \exp(i\omega t)$ . Writing  $\mathbf{u} = (u, w)$  in 2D and  $\mathbf{u} = (u, w, v)$  in 3D, and discretizing Eq. (27) by the FD method on the staggered grid shown in Fig. 6, we obtain a set of discretized equations for determining the monochromatic solutions. The problem of solving the set of the discretized equations is then formulated as one of an eigenvalue problem. If we define a vector  $\mathbf{Z}$ , the components of which represent all the field variables (displacements) at the grid points, then the set of the discretized equations is written as

$$\sum_{\beta} H_{\alpha\beta} Z_{\beta} = \Omega Z_{\alpha}, \quad (35)$$

where,  $\Omega = \omega^2$ , with the matrix of the coefficients  $\mathbf{H}$  being symmetric. Discretizing the governing equations introduces a cutoff length scale and, hence, a cutoff frequency in the simulations, which do not exist in the

continuum equations (27). We neglect such difference between the discrete and continuous system (which can be reduced by decreasing the size of the blocks in the computational grid).

To determine whether an eigenstate is localized or extended in the limit of large system sizes, we calculate the minimum positive *Lyapunov exponent*  $\gamma_m$ , which is simply the inverse of the localization length  $\xi$ . The most suitable numerical method for directly computing the localization properties of noninteracting disordered media is, perhaps, the transfer-matrix (TM) technique, using a strip (bar) in two (three) dimensions, with periodic boundary conditions in the transverse direction(s). To formulate the TM computations, we rewrite the discretized equations in the following form:

$$\begin{pmatrix} \mathbf{Z}_{n+1} \\ \mathbf{Z}_n \end{pmatrix} = \mathbf{T}_n \begin{pmatrix} \mathbf{Z}_n \\ \mathbf{Z}_{n-1} \end{pmatrix}, \quad (36)$$

where  $\mathbf{Z}_n$  is the vector that contains the values of (the discretized) displacements  $\mathbf{u}(\mathbf{x})$  in slice number  $n$  in the 2D strip or the 3D bar. For 2D media, for example,  $\mathbf{Z}_n$  contains  $2M$  components because every grid point is characterized by two displacements ( $u, w$ ). Thus, the vectors on both sides of Eq. (36) contain  $4M$  components and, as a result,  $\mathbf{T}_n$  is a  $4M \times 4M$  matrix, resulting in  $4M$  Lyapunov exponents, half ( $2M$ ) of which are independent as they appear in pairs,  $(\gamma, -\gamma)$ . The inverse of the minimum Lyapunov exponent is the localization length that we wish to compute.

Because the discretized equations are defined on a staggered grid, and we have a set of coupled equations for each grid point, instead of a single equation (because we solve a vector equation), the slices for the TM steps should be defined carefully. In 2D we impose the boundary condition on one side of the strip and then move forward in the (longitudinal)  $x$  direction by multiplication of the TM matrices. To do this, we define the set of two lines,  $x = i$  and  $x = i + \frac{1}{2}$ , as a single slice. All the variables in the slice  $(i + 1, i + 1 + \frac{1}{2})$  are then computed, if one knows the values in the slices  $(i, i + \frac{1}{2})$  and  $(i - 1, i - 1 + \frac{1}{2})$ . In the same way, a boundary condition is imposed on one end plane of the bar, and a 3D slice is defined as being composed of two planes,  $z = k$  and  $z = k + \frac{1}{2}$ .

We used  $M \times L$  strips and  $M \times M \times L$  bars, where  $M$  is the transverse dimension and  $L$  the length. If  $N = dM^{d-1}$ , where  $d = 2$  and  $3$ , then the dimensions of the TM in Eq. (36) and number of the Lyapunov exponents are  $2N$ . Therefore, the simulations start with  $2N$  initial orthonormal vectors, corresponding to the dimension of the TM, taken to be  $\mathbf{v} = (1, 0, \dots, 0)^T$ ,  $(0, 1, 0, \dots, 0)^T$  and so on, where  $T$  denotes the transpose operation. Because of being multiplied by the successive TMs, the directions of the initial vectors change. The Lyapunov exponents are then the logarithm of the trace of the matrix,  $\mathbf{V} = [\mathbf{T}(\mathbf{T}^T)]^{1/2n}$ , where  $\mathbf{T} = \mathbf{T}_n \mathbf{T}_{n-1}, \dots, \mathbf{T}_1$ . Then the direction that corresponds to the largest Lyapunov is the direction of the eigenvector that corresponds to the largest eigenvalue of the matrix  $\mathbf{V}$ .

However, after a few steps, the information about all the Lyapunov exponents but the largest one will be lost in the numerical noise and round-off. To avoid this difficulty we implemented the Gram–Schmidt (GS) orthogonalization after every two steps of the TM iterations. The number of steps after which the GS orthogonalization should be applied depends on the model, and may actually be estimated [41,42].

Figure 7 presents the inverse of the scaled localization length,  $\Lambda = (M\gamma_m)^{-1}$  in the 2D media as a function of  $\Omega = \omega^2$  for the disorder parameters,  $W_\lambda = W_\mu = 0.99$  and  $\lambda_0 = \mu_0 = 1.0$ , and several  $M$ , the width of the strips used in the TM computations. The results have an estimated error of 0.1%. At first glance, it appears that  $\Lambda$  decreases by increasing the width, implying that it vanishes in the limit of very large system size and, therefore, all the wave states are localized in the 2D disordered media that we studied, up to the frequencies that were considered.

However, a closer inspection of Fig. 7 indicates an intriguing possibility. It appears that for  $\Omega > 10$ ,  $\Lambda^{-1}$  exhibits an  $M$ -dependence, whereas for  $\Omega < 10$  the dependence on  $M$  is weak, if it exists at all. The difference indicates that the possibility of the existence of extended states cannot be ruled out in such 2D media. If such states do exist, it would be consistent with the prediction of the RG calculations described in Sect. 4 for 2D media, which did predict the existence of such states in 2D.

In 3D media, however, the Lyapunov exponent behaves differently. Figure 8 displays the results for the inverse of the (rescaled) localization length  $\Lambda^{-1}$  for the same disorder parameters as those in the 2D media. The results for all values of the width  $M$  of the 3D bars (used in the TM computations) intersect one another at a particular critical frequency  $\Omega_c$ . For  $\Omega < \Omega_c$  the rescaled Lyapunov exponent decreases with increasing  $M$ , i.e., one has extended states.

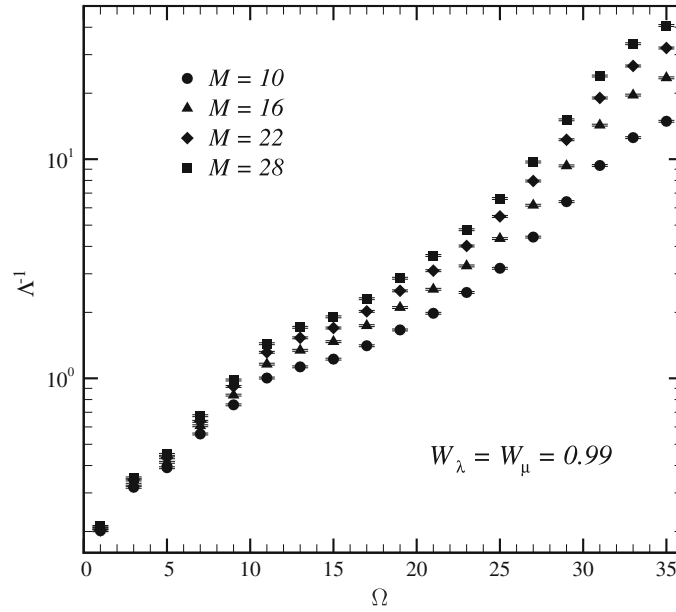


**Fig. 7** Inverse of the scaled localization length  $\Lambda$  of the 2D model, obtained with an error of about 0.1%

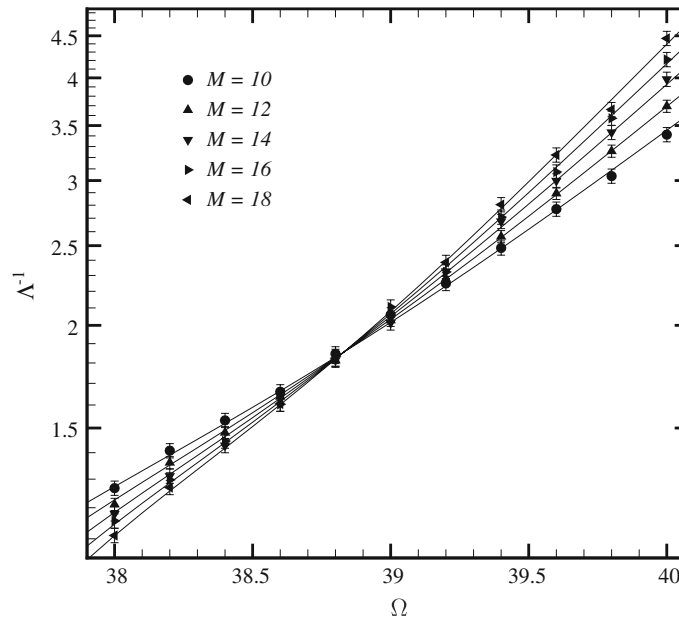


**Fig. 8** Inverse of the scaled localization length  $\Lambda$  of the 3D model for  $W_\mu = W_\lambda = 0.99$ , obtained with an error of about 2%

### 6 Probing the difference between correlated and uncorrelated media

In this section we describe the results of numerical simulation of the propagation of acoustic waves that enable us to distinguish disorder with long-range correlations from random (uncorrelated) heterogeneity [43]. As in the previous sections, two types of heterogeneous media are considered. In one type, the spatial distribution of the local bulk moduli contain long-range correlations with a power-law, nondecaying correlation function. The correlation length is, therefore, as large as the linear size of the medium. In the second type of heterogeneous media the correlation length is decreased, up to the linear size of the blocks in the computational grid and, therefore, the distribution of the local bulk moduli is uncorrelated (white noise), but with the same variance as that of the correlated media.

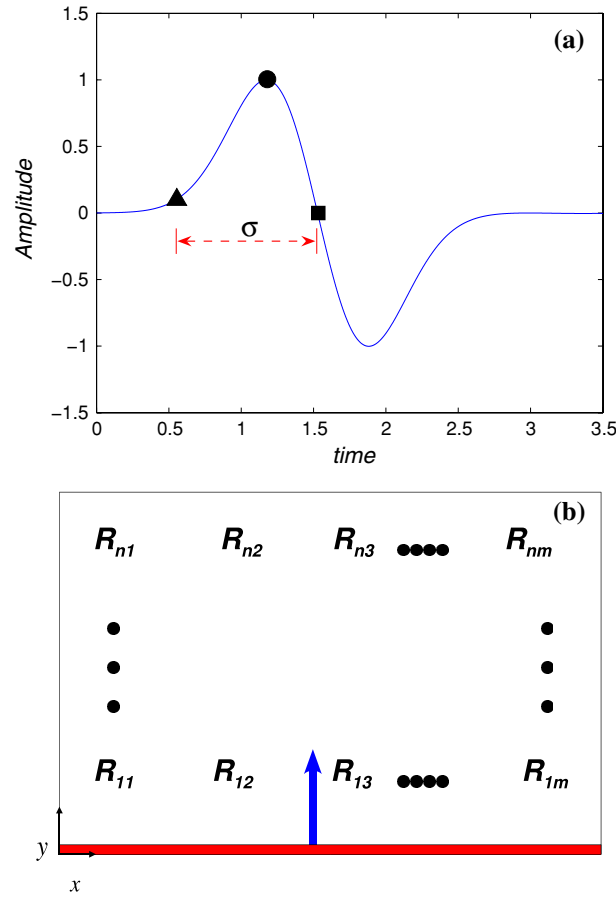


**Fig. 9** **a** The shape of the wave at the source. *Triangles, circles, and squares* denote, respectively, the time at which the amplitude is 10% of its peak value (shown by the *circle*), the peak position, and the first zero-crossing.  $\sigma$  is the width of the coherent wave front. **b** The distribution of the receivers. The source is at the bottom of the system at  $y = 0$ . *Arrow* indicates the main direction of wave propagation

One finds that [43] there are fundamental differences between wave propagation in the two types of heterogeneous media. In particular, the evolution of four distinct characteristics of the waves, namely, the amplitude of the coherent wave front (CWF), its width, the spectral densities and the scalogram (wavelet transformation of the waves' amplitudes at different scales and times), and the dispersion relations (DRs) are completely different for uncorrelated and correlated media. Such differences point to wave propagation experiments that can detect important characteristics of the heterogeneities that a medium may contain, and help distinguish correlated disordered media from the uncorrelated ones.

Based on preliminary simulations in 2D using  $L_x \times L_y$  grids, we used  $L_x = 400$  and  $L_y = 4,000$  and  $8,000$  ( $L_x$  and  $L_y$  are in units of the length of the individual blocks in the computational grid). The main direction of wave propagation was taken to be the  $y$  direction, while periodic boundary conditions were imposed in the  $x$  direction which, due to the large sizes of the computational grid, did not distort the nature of the wave propagation. The acoustic wave equation, Eq. (3), was solved by the numerical technique described in Sect. 3. To compute the amplitude decay and the frequency-dependence of the waves during their propagation, we collect the numerical results at receivers (grid points) that are distributed evenly throughout the grid, along the main direction of the wave propagation. The simulations indicated that averaging the results over 85 realizations of the system suffices for obtaining results that will not change if we take a larger number of realizations.

Figure 9 shows the shape and cycle of the wave at the source (at  $y = 0$ ) that propagates throughout the heterogeneous medium. As the waves propagate in the medium, their multiple scattering generates many cycles of seemingly irregular oscillations. Such irregularities disappear for the averaged wave, i.e., one that represents an average over all the realizations. The first one of such cycles of the oscillations, or the first few of them—often

called the CWF [44]—is an important characteristic of a propagating wave. An alternative definition of the CWF is that it is that part of the wave that remains intact after averaging over all the realizations.

The value of  $\psi_c$  for the first peak (in the CWF) and the time (location) at which it occurs are also important characteristics of the propagation process. During the waves' propagation, the numerical value of  $\psi_c$  for the CWF decreases, while the front's width  $\sigma$  increases. Thus, we also focus on the decay of  $\psi_c$  and the shape of the CWF, as characterized by  $\sigma$ . As described below, they generate distinct "signatures" that contain information on the spatial distribution of  $K(\mathbf{x})$ . Hence, we compute the time-dependence of  $\psi_c$  at a fixed distance from the source. Then, as described below, from a sequence of the numerical data at every receiver, a qualitative picture of the evolution of the CWF versus the receivers' distance from the source emerges.

Thus, to study quantitatively the evolution of the CWF, we characterize it by three properties: its peak value  $\psi_c$ , the time at which  $\psi$  attains 10% of the peak value  $\psi_c$  (the 10% is rather arbitrary, and only represents a rough measure of where the wave field becomes relatively significant), and its *first zero-crossing*—the time at which  $\psi(\mathbf{x}, t)$  vanishes for the *first time* after the first peak. Then, the width  $\sigma$  of the CWF is defined as the time between the first zero-crossing and when the coherent wave's  $\psi(\mathbf{x}, t)$  is 10% of the peak value  $\psi_c$ . These are all shown in Fig. 9. The manner by which these properties evolve depend strongly on the spatial distribution of the elastic constant  $K(\mathbf{x})$ . As they can be measured in practice, they provide important information on the spatial distribution of  $K(\mathbf{x})$ .

To characterize the propagation of acoustic waves more precisely, we need a tool that enables us to obtain the frequency content of the time series  $\psi(\mathbf{x}, t)$ —a process often referred to as the *time–frequency analysis*. The goal of such analysis is to expand the time series into the sum of wavelike forms, the time–frequency properties of which are adapted to the time series' local structure. The continuous wavelet transform (CWT) of a time series  $s(u)$  is one such tool, which is defined by the following integral transform [45]:

$$\hat{s}(\lambda, t) = \int_{-\infty}^{\infty} s(u) \bar{\Psi}_{\lambda, t}(u) du, \quad (37)$$

where

$$\Psi_{\lambda, t}(u) = \frac{1}{\sqrt{\lambda}} \Psi\left(\frac{u-t}{\lambda}\right) \quad (38)$$

represents a family of functions referred to as the wavelets. Here,  $\lambda$  is a scale parameter,  $t$  a time (location) parameter representing the translation of the wavelet at different times, and  $\bar{\Psi}$  is the complex conjugate of  $\Psi$ .  $\Psi(u)$  is often referred to as the *mother wavelet*. Clearly, changing  $\lambda$  has the effect of dilating ( $\lambda > 1$ ) or contracting ( $\lambda < 1$ ) the function  $s(u)$ . On the other hand, varying  $t$  has the effect of analyzing the function  $s(u)$  around different points at times  $t$ . When  $\lambda$  increases, the wavelet becomes more spread out and takes only the long-time behavior of  $s(u)$  into account, and vice versa. Therefore, the CWT provides a flexible time-scale window that narrows when focusing on small-scale features, and widens on large-scale features. Note that  $\Psi_{\lambda, t}(u)$  has the same shape for all values of  $\lambda$ .

The CWT, as defined by Eq. (37), is a continuous transformation because the scale and time parameters,  $\lambda$  and  $t$ , assume continuous values. In our analysis we use continuous complex Morlet wavelet [45], which is well-known in geophysical applications, in order to obtain information about the instantaneous frequency attributes of the propagating waves, and to determine which part of the waves is scattered more during the propagation. The Morlet wavelet is given by

$$\Psi(t) = \pi^{-1/4} \exp[-(i\omega_0 t - t^2/2)], \quad \omega_0 \geq 5. \quad (39)$$

Since the Morlet wavelet is a complex function, it enables one to extract information about both the amplitude and phase of the process being analyzed. As an example, we show in Fig. 10 the CWT of  $S_0(t)$  given by Eq. (25) (using the Morlet wavelet). The vertical axis  $\lambda$  is set to,  $\lambda = 2T_s$ , where  $T_s = 1/\nu_s$ , with  $T_s$  and  $\nu_s$  being the mean period and frequency, respectively. The horizontal axis is the dimensionless time, while the colors show the intensity of  $|\hat{S}_0(\lambda, t)|^2$  at different times and scales. Using such plots—usually called the *scalogram*—we determine the positions of the frequency modes on the time axis (i.e., the time at which they arrive at a given receiver) and, hence, determine which frequency attributes move faster than the others, and how the heterogeneities in the medium affect them.

We have also computed the DRs for propagation of the waves in both correlated and uncorrelated media [46], i.e., the relation between the angular frequency  $\omega$  and the wave vector  $k$  ( $k = 2\pi/\chi$ , where  $\chi$  is the

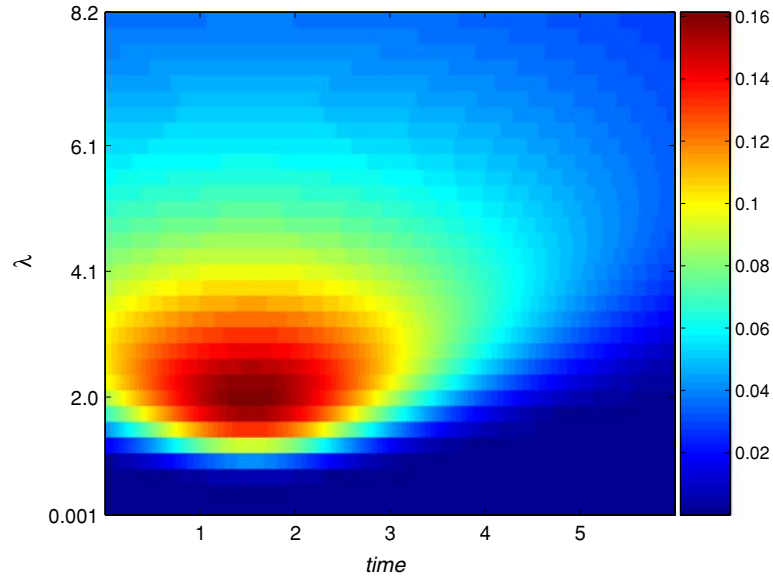


**Fig. 10** Scalogram (wavelet transform) of the source function  $S_0(t)$ , given by Eq. (25)

wavelength).  $\omega(k)$  characterizes wave attenuation in a system. We have shown [43] them to be very different for uncorrelated (or those with short-range correlations) and those with long-range correlations, hence providing another signature of such correlations in a heterogeneous medium.

As the first example, consider acoustic wave propagation in a medium in which the bulk modulus  $K(\mathbf{x})$  follows a statistical distribution with a power-law, nondecaying correlation function (see Eq. 5), with a Hurst exponent,  $H = \rho - 1$ . We compare the results with those for an uncorrelated medium, but with the same variance as that of the correlated medium. In an uncorrelated medium the quantity  $\psi_c$  of the CWF decays as a *power law* in the distance  $d$  between the source and the receiver [47], at least if the distribution of  $K(\mathbf{x})$  is not extremely broad. The same is true [44] about wave propagation in granular materials which represent unconsolidated porous media. However, the decay of  $\psi_c$  in a heterogeneous medium with long-range correlations is much faster, and takes on an exponential form—similar to electron localization. Thus, the exponential decay of  $\psi_c$  of the CWF is the first “signature” of the existence of long-range correlations in a disordered medium, and in particular the nondecaying correlations that are generated by the power-law, nondecaying correlation function. Figure 11 confirms the exponential decay of the amplitude  $\psi_c$  in three heterogeneous media, and compares them with that in an uncorrelated medium but with the same variance.

Another feature of wave propagation is the broadening of the width  $\sigma$  of the CWF during the propagation. In uncorrelated media, the width of the coherent part increases with  $d$  as a power law [44], where  $d$  is the distance between the source and the receivers. However, in correlated media in which the spatial distribution of the bulk modulus  $K(\mathbf{x})$  is characterized by a power-law, nondecaying correlation function, the dependence of the width  $\sigma$  of the CWF on the source-receiver distance  $d$  is *exponential*, fundamentally different from that of uncorrelated media. This is demonstrated in Fig. 12, where we present the width of the CWF for both types of heterogeneous media. Thus, the exponential dependence of the width  $\sigma$  of the CWF may be considered as the second signature of long-range correlations in heterogeneous media.

The third important feature of the waves is the frequency-dependence of their power spectrum during the propagation. It is well-known that in an uncorrelated medium the high-frequency modes scatter more efficiently than the low-frequency ones. Figure 13 presents the (normalized) power spectra of the waves that were received by 4 different sets of receivers located along the propagation direction (receivers  $R_{1i}$  to  $R_{4i}$  shown in Fig. 9b). The results, computed for the first few cycles of the amplitudes, represent averages over many realizations. As Fig. 13 indicates, the shape of the power spectrum changes when one computes or measures it at various distances from the source. The ratio of low- and high-frequency modes increases as the source-receiver distance  $d$  increases, hence indicating that, in *uncorrelated media*, the waves lose their high-frequency modes faster than the low-frequency ones.

In the correlated media that we consider, the evolution of the power spectrum is, however, different. Figure 14 presents the (normalized) power spectra for  $H = 0.3$  and  $0.75$  ( $\rho = 1.3$  and  $1.75$ ) for the same

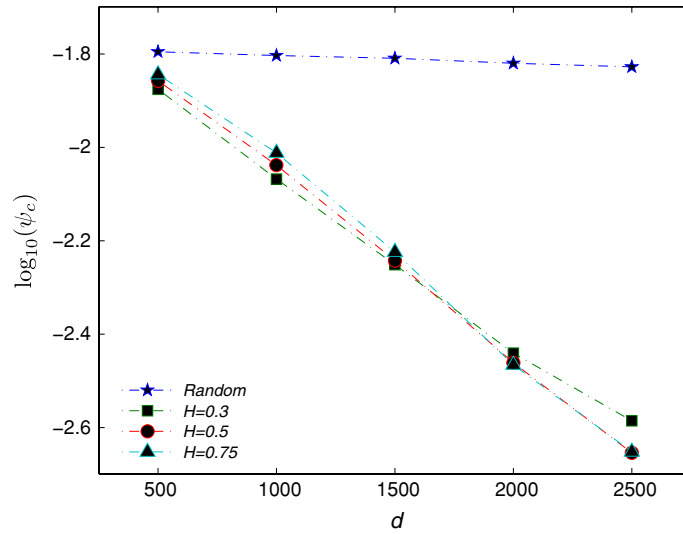


**Fig. 11** Dependence of the coherent wave amplitude  $\psi_c$  (the first peak in the plot of  $\psi(\mathbf{x}, t)$  versus time) on the distance  $d$  between the source and the receivers. The local bulk moduli are distributed according to a correlated distribution with the Hurst exponent  $H$

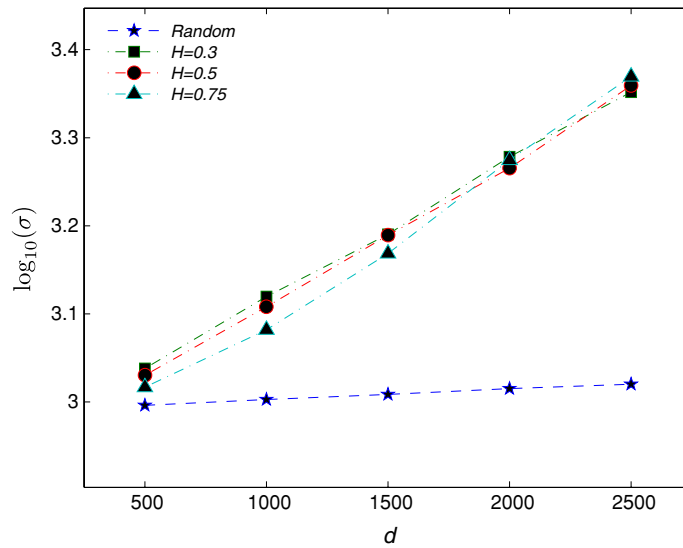


**Fig. 12** Dependence of the width  $\sigma$  of the coherent wave front on the distance  $d$  between the source and the receivers, in an uncorrelated medium, as well as in a medium in which the local bulk moduli are distributed according to a correlated distribution with a Hurst exponent  $H$

receivers as in Fig. 13. The changes in all the spectra for each frequency is approximately the same as for all other frequencies. Thus, when long-range correlations are present in the spatial distribution of the local bulk moduli, the low-frequency modes are scattered just as efficiently and fast as the high-frequency ones. Such a difference between the two types of power spectra may also be considered as evidence of long-range correlations in a disordered medium.

To make the distinction between the uncorrelated and correlated media clearer, we computed [43] the scalogram (the CWT of the first few cycles of the amplitude) of the waves arriving at various receivers, in order to determine their instantaneous frequency distribution during the propagation. Figure 15 presents the scalogram of the wave front received by four receivers along the  $y$  direction (the main direction for wave propagation), namely,  $R_{12}$ ,  $R_{22}$ ,  $R_{32}$ , and  $R_{42}$ , from top to bottom, respectively. The different colors show the intensity of  $|\hat{\psi}(\lambda, t)|^2$ . In the top scalogram, the intensity in most of the diagram for  $3 < t < 10$  is essentially zero (no wave has arrived there yet). But, in the scalogram at the bottom, which is for the waves that have arrived

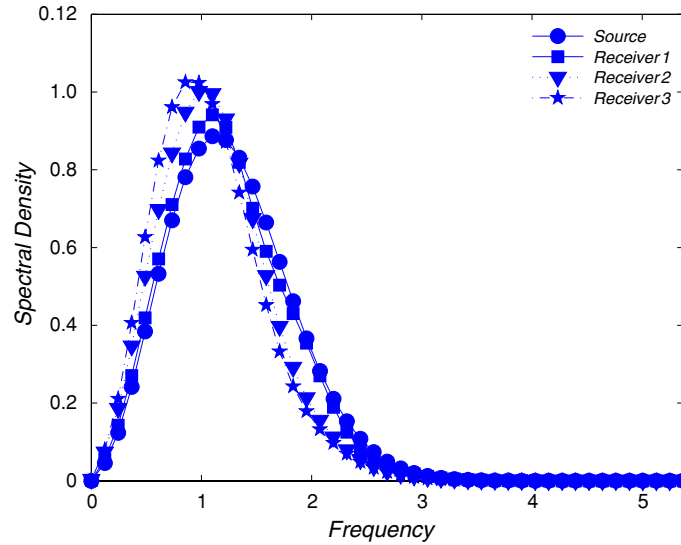


**Fig. 13** Normalized spectral density of the wave front at the source, and at three different receivers located along the  $y$ -direction (the main direction of wave propagation), in an uncorrelated medium

at the farthest receiver, nonzero intensities appear in the same region. As seen clearly, after the main part there are some zones with nonzero intensity, which indicate that the main part of the waves lose some of their high-frequency attributes and, therefore, the lost frequencies arrive at the receiver(s) after a delay. This is consistent with what is presented in Fig. 13 for the spectral density of the same waves.

But, the scalogram for the case of a medium with a correlated distribution of the local bulk moduli is completely different. Figure 16 presents the scalogram at the same receivers with the Hurst exponent  $H = 0.3$  ( $\rho = 1.3$ ). The features of the evolution of these scalogram are in sharp contrast with those shown in Fig. 9. All the receivers receive all the frequencies after the main part of the wave, hence indicating that essentially simultaneous scattering of all the frequency modes is one major feature of wave propagation in heterogeneous media in which the spatial distribution of the local elastic moduli contains long-range correlations. This important difference between the scalogram of uncorrelated and correlated media, which can be computed rather straightforwardly in practical applications of wave propagation, may also be considered as another “signature” of the existence of such correlations in the local elastic moduli.

The distinction between uncorrelated and correlated media can perhaps be demonstrated more clearly by introducing a cutoff length scale  $\ell$  for the correlations in the bulk modulus  $K(\mathbf{x})$ . The correlations are preserved over length scales  $L < \ell$ , but are lost for  $L > \ell$ . Naturally, the cutoff length scale  $\ell$  must be larger than the linear size of the blocks in the computational grid. Fixing all the parameters and varying only  $\ell$  should indicate better the effect of the correlations and their extent.

Figure 17 presents the power spectrum of the waves for two cutoff lengths. The results were computed for receivers  $R_{j1}$ ,  $R_{j2}$ ,  $R_{j3}$  and  $R_{j4}$ , and then were averaged over  $j$  in each case, with  $j = 1, 2$  and  $3$ . The top figure shows the power spectra for  $\ell = 400$ , a relatively short cutoff length. Thus, for this cutoff the medium appears like an uncorrelated one at large scales and, therefore, the spectral density is also similar to that of an uncorrelated medium shown in Fig. 13. By increasing  $\ell$ , the shapes of the power spectra at different times (receivers) become increasingly similar to that of a medium with long-range correlations in the spatial distribution of  $K(\mathbf{x})$ . Thus, there is a transition from an uncorrelated to a correlated medium with long-range correlations. Similar effects can also be seen [43] in the behavior of the width  $\sigma$  of the CWF.

These results also point to an important consideration in the practical applications of seismic wave propagation in heterogeneous rock, and the geophysical interpretation of the results. As shown above, the cutoff length scale  $\ell$ —which is just the correlation length  $\xi_K$  for the local elastic constants—plays an important role in the transition from an uncorrelated medium to a correlated one. At the same time, there is a relation between  $\xi_K$  and the range of the wavelengths that can be used in a seismic exploration of heterogeneous porous media. If  $\xi_K$  is smaller than the wavelength used in the exploration, the frequency-dependence of the coherent wave’s spectral density will be similar to that of uncorrelated media shown in Fig. 13. But if the wavelength is smaller than  $\xi_K$ , one should find a transition in the spectral density, similar to what we presented above with the various

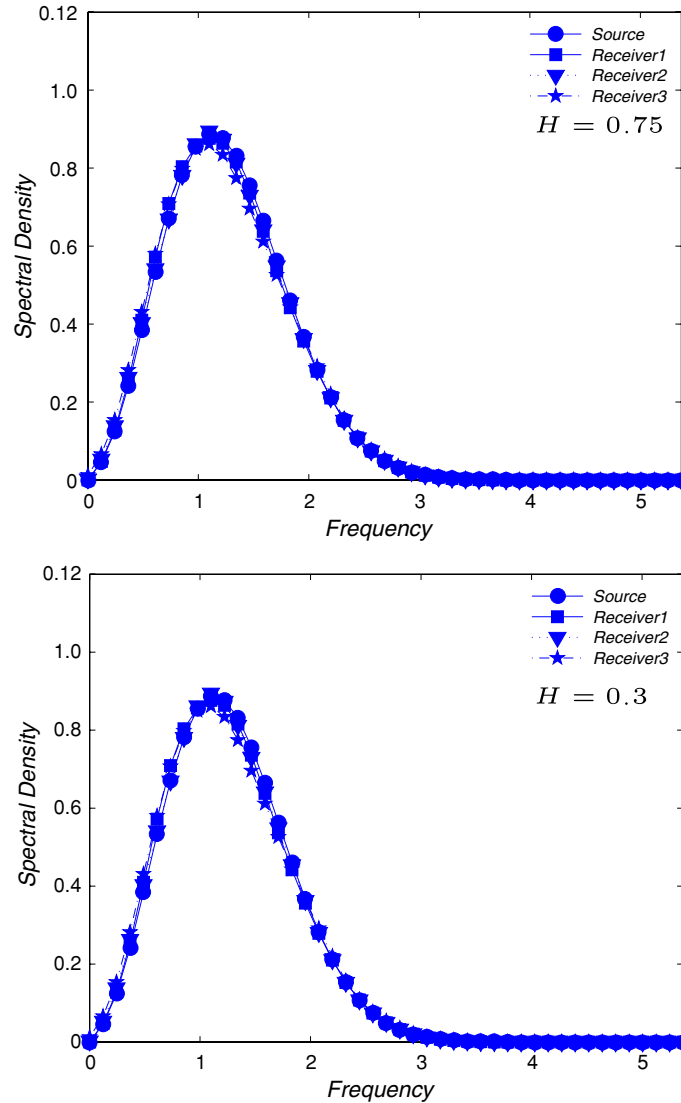


**Fig. 14** Same as in Fig. 13, but in isotropic correlated media with a Hurst exponent  $H$

cutoff lengths  $\ell$ . Thus, in any seismic exploration one should use a *range* of frequencies (wavelengths), in order to be able to discern the effect of the correlations in the seismic traces, and possibly detect a signature of the spatial distribution of the medium's local elastic constants.

## 7 Summary

The work described in this paper demonstrates that, depending on the nature of the disorder, acoustic and elastic waves in strongly disordered media can be localized or delocalized in *any* spatial dimension. These results have important practical implications. For example, as pointed out in the Introduction, in order for seismic records to contain meaningful information on the geology and content of a natural porous formation of linear size  $L$ , the localization length  $\xi$  must be larger  $L$ . Otherwise, propagation and scattering of such waves can provide information on the formation only up to length scale  $\xi$ ; one cannot delineate meaningful information at larger length scales. The localization length  $\xi$  is, clearly, a function of the medium's spatial dimension, the exponent  $\rho$  and amplitude  $W_\rho$ , and other relevant physical parameters of the system. The determination of  $\xi$  as a function of such parameters remains a major numerical task.

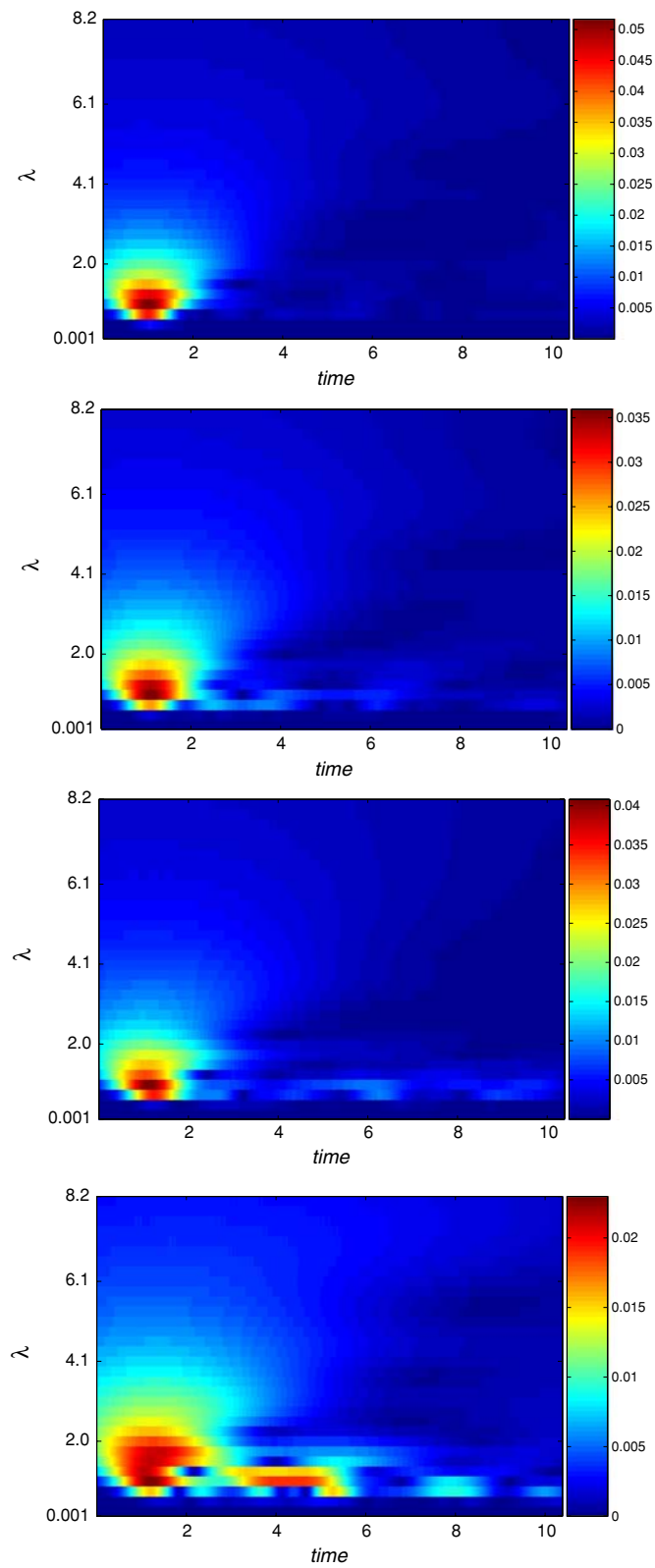


**Fig. 15** Scalogram (wavelet transform) of the wave front, received by four different receivers, located along the direction of wave propagation, in an uncorrelated medium. The diagrams show, from *top to bottom*, the results for the receivers closest to, and farthest from, the source

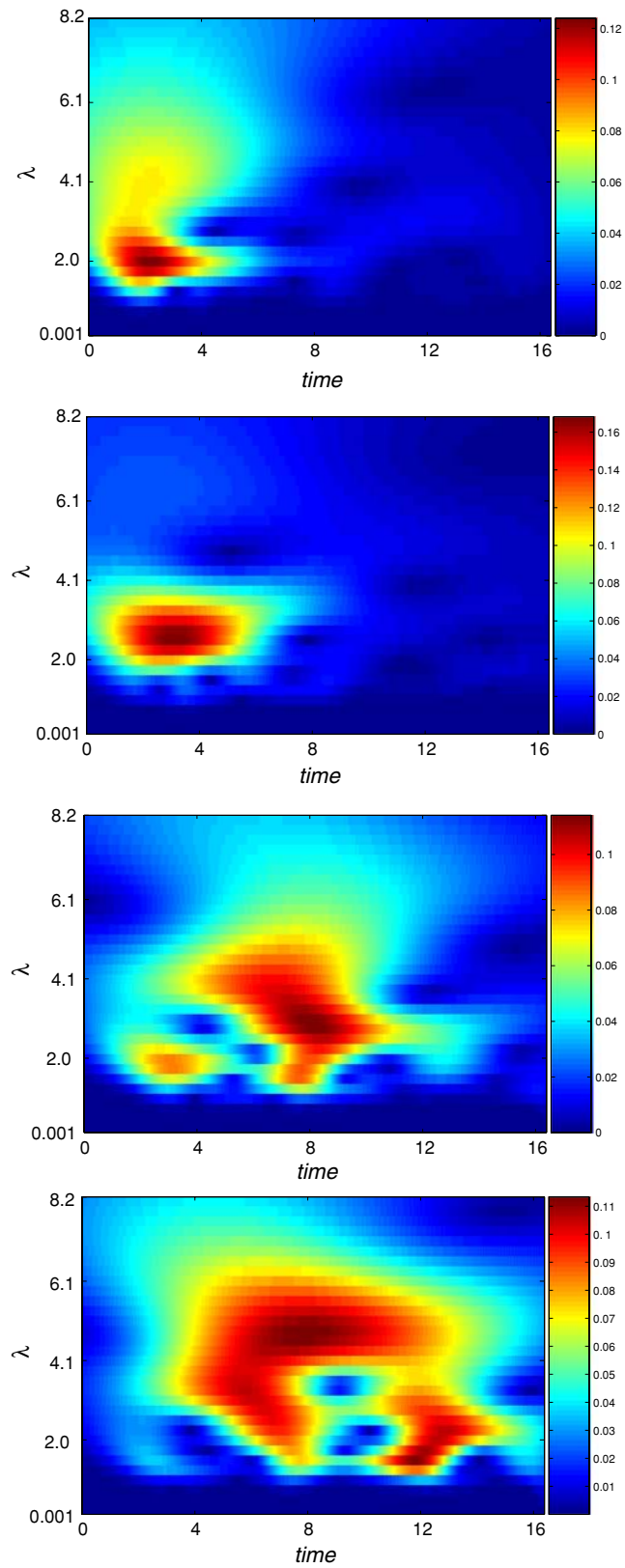


**Fig. 16** Same as in Fig. 15, but for an isotropic correlated medium with a correlated distribution of the local bulk moduli with the Hurst exponent  $H = 0.3$

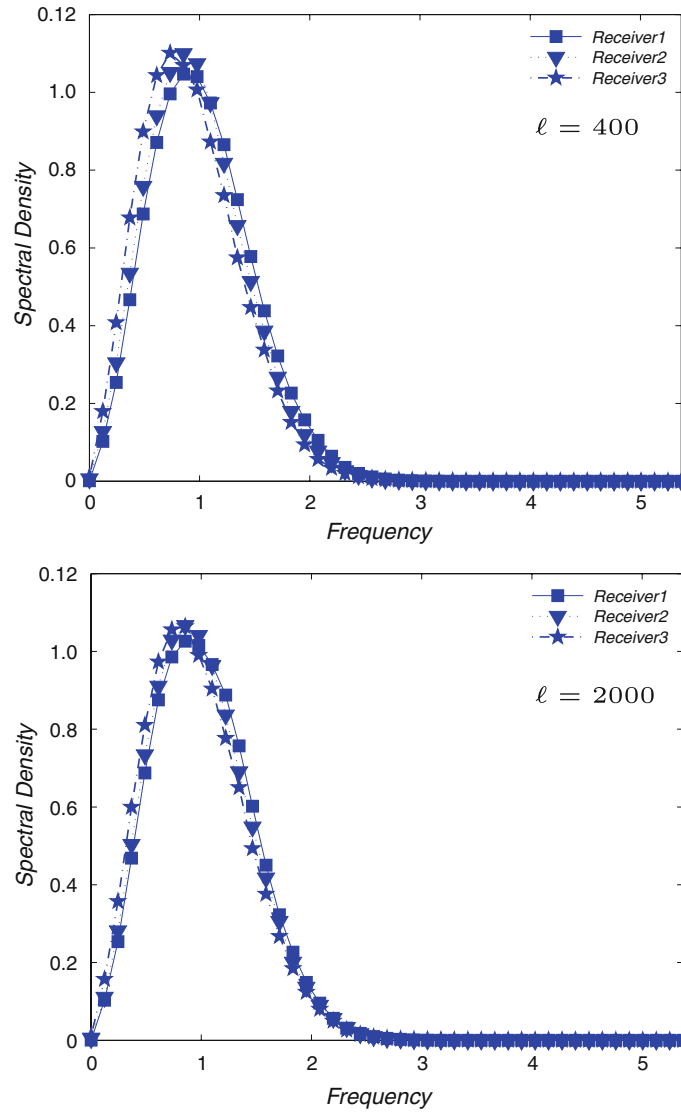


**Fig. 17** The normalized spectral density of the wave front at three different receivers, as described in the text. The results are for an anisotropic medium with a correlated distribution of the local bulk moduli with a Hurst exponent  $H = 0.3$ , and a cutoff length  $\ell$

Localization of elastic waves also has important implications for predicting when an earthquake may occur. If the station that collects the data emanating from the vicinity of an earthquake hypocenter is at a distance from the center which is larger than the localization length  $\xi$ , analysis of the seismic data, such as the vertical velocity of earth, will not provide any insight into when an earthquake may occur. This was recently demonstrated by our work [48], based on the analysis of extensive data for vertical velocity of earth for several large and intermediate size earthquakes around the world.

We also described strong numerical evidence that crucial characteristics of the waves, including their amplitude decay, width, spectral density, and scalogram, are fundamentally different for uncorrelated and correlated disordered media. These aspects of wave propagation help one to correctly interpret seismic data. They also help one to detect signatures of specific types of disorder in the heterogeneous media of the type that we studied in this paper that are actually abundant in the nature.

We have also shown [49] that power-law correlations of the type that we consider in this paper give rise to rough, self-affine wave fronts (WFs) in heterogeneous media. The self-affinity of the WFs is characterized by a roughness exponent  $\alpha$ , which is estimated as follows. We compute the second-order front-front correlation function, defined by

$$C(r) = \langle [d(x) - d(x+r)]^2 \rangle, \quad (40)$$

where  $d(x)$  is the position of the WF. For example, in 2D and at a given  $x$ ,  $d(x)$  is the WF distance along the  $y$ -direction, the main direction of wave propagation, from the first row at  $y = 0$ , and the averaging, for each value of  $r$  (also a point on the WF), is over all values of  $x$ . For a self-affine rough front, one must have

$$C(r) \sim r^{2\alpha}, \quad (41)$$

where  $\alpha$  is called the roughness exponent. We showed [49] that in all the cases one has

$$\alpha = H = \rho - 1. \quad (42)$$

That is, the WF roughness exponent—a *dynamical property* of the medium—is equal to the Hurst exponent—a *static property* of the medium that characterizes the spatial distribution of its local elastic moduli. This opens up the possibility of determining the Hurst exponent  $H$  (or, equivalently, the exponent  $\rho$ ) in a laboratory experiment. Equation (42) is, in fact, a direct consequence of localization of elastic waves.

**Acknowledgments** The work of R.S. and S.M.V.A. was supported by the NIOC. M.R.R.T. would like to thank the *Knowledge Archive* funding for financial support. M.S. would like to express his appreciation and gratitude to Professor Joe D. Goddard for his mentorship at the early stages of his career, and for a friendship that has lasted for a quarter of a century.

## References

1. Bleistein, N., Cohen, J.K., Stockwell, J.W. Jr.: *Mathematics of Multidimensional Seismic Imaging, Migration, and Inversion*. Springer, New York (2001)
2. Sahimi, M.: *Heterogeneous Materials II*. Springer, New York (2003)
3. Adler, P.M., Thovert, J.-F.: *Fractures and Fracture Networks*. Kluwer, Amsterdam (1999)
4. Sahimi, M.: *Flow and Transport in Porous Media and Fractured Rock*. Wiley-VCH, Berlin (1995)
5. Sahimi, M., Tajer, S.E.: *Phys. Rev. E* **71**, 046301 (2005)
6. Sheng, P.: *Introduction to Wave Scattering, Localization and Mesoscopic Phenomena*. Academic, San Diego (1995)
7. Anderson, P.W.: *Phys. Rev.* **109**, 1492 (1958)
8. Mott, N.F., Twose, W.D.: *Adv. Phys.* **10**, 107 (1961)
9. Abrahams, E., Anderson, P.W., Licciardello, D.C., Ramakrishnan, T.V.: *Phys. Rev. Lett.* **42**, 673 (1979)
10. Wegner, F.: *Nucl. Phys. B* **180**(FS2), 77 (1981)
11. Kramer, B., MacKinnon, A.: *Rep. Prog. Phys.* **56**, 1469 (1993)
12. Anderson, P.W.: *Phil. Mag. B* **52**, 505 (1985)
13. Sheng, P., Zhang, Z.Q.: *Phys. Rev. Lett.* **57**, 1879 (1986)
14. Arya, K., Su, Z.B., Birman, J.L.: *Phys. Rev. Lett.* **57**, 2725 (1986)
15. Soukoulis, C.M., Economou, E.N., Grest, G.S., Cohen, M.H.: *Phys. Rev. Lett.* **62**, 575 (1989)
16. Wiersma, D.S., Bartolini, P., Lagendijk, A., Righini, R.: *Nature* **390**, 671 (1997)
17. Martin, P.C., Siggia, E.D., Rose, H.A.: *Phys. Rev. A* **8**, 423 (1973)
18. Cohen, S.M., Machta, J., Kirkpatrick, T.R., Condat, C.A.: *Phys. Rev. Lett.* **58**, 785 (1987)
19. Foret, M., Courtens, E., Vacher, R., Suck, J.B.: *Phys. Rev. Lett.* **77**, 3831 (1996)
20. Ye, Z., Alvarez, A.: *Phys. Status Solidi B* **214**, 285 (1999)
21. Gupta, B.C., Ye, Z.: *Phys. Rev. E* **67**, 036606 (2003)
22. Robin, T., Souillard, B.: *Physica A* **193**, 79 (1993)
23. Baluni, V., Willemsen, J.: *Phys. Rev. A* **31**, 3358 (1985)
24. Maynard, J.D.: *Rev. Mod. Phys.* **73**, 401 (2001)
25. Larose, E., Margerin, L., Tiggelen, B.A. van, Campillo, M.: *Phys. Rev. Lett.* **93**, 048501 (2004)
26. Schwartz, T., Bartal, G., Fishman, S., Genack, A.Z.: *Nature* **446**, 52 (2007)
27. Kuhl, U., Izrailev, F.M., Krokhn, A.A.: *Phys. Rev. Lett.* **100**, 126402 (2008)
28. Ishimaru, A.: *Wave Propagation and Scattering in Random Media*. Oxford University Press, Oxford (1997)
29. Shahbazi, F., Bahraminasab, A., Vaez Allaei, S.M., Sahimi, M., Rahimi Tabar, M.R.: *Phys. Rev. Lett.* **95**, 165505 (2005)
30. Bahraminasab, A., Vaez Allaei, S.M., Shahbazi, F., Sahimi, M., Niry, M.D., Rahimi Tabar, M.R.: *Phys. Rev. B* **75**, 064301 (2007)
31. Bahraminasab, A., Esmailpour, A., Vaez Allaei, S.M., Shahbazi, F., Sahimi, M., Rahimi Tabar, M.R.: *Phys. Rev. B* **77**, 216302 (2008)
32. Esmailpour, A., Esmailpour, M., Sheikhan, A., Elahi, M., Rahimi Tabar, M.R., Sahimi, M.: *Phys. Rev. B* **78**, 134206 (2008)
33. Kneib, G., Kerner, C.: *Geophysics* **58**, 576 (1993)
34. Voss, R.F.: In: Earnshaw, R.A. (ed.) *Fundamental Algorithms for Computer Graphics*, NATO Advanced Study Institute, Series E: Applied Science, vol. 17, p. 805. Springer, Heidelberg (1985)
35. Pang, N.-N., Yu, Y.-K., Halpin-Healy, T.: *Phys. Rev. E* **52**, 3224 (1995)
36. Makse, H.A., Havlin, S., Schwartz, M., Stanley, H.E.: *Phys. Rev. E* **53**, 5445 (1996)
37. Hamzehpour, H., Sahimi, M.: *Phys. Rev. E* **73**, 056121 (2006)
38. Saperhrinia, R., Bahraminasab, A., Sahimi, M., Rahimi Tabar, M.R.: *Phys. Rev. B* **77**, 014203 (2008)

39. Sepehrinia, R., Rahimi Tabar, M.R., Sahimi, M.: *Phys. Rev. B* **78**, 024207 (2008)
40. Sahimi, M., Vaez Allaei, S.M.: *Comput. Sci. Eng.* **10**(3), 66 (2008)
41. Pichard, J.L., Sarma, G.: *J. Phys. C* **14**, L127 (1981)
42. MacKinnon, A., Kramer, B.: *Z. Phys. B* **53**, 1 (1983)
43. Vaez Allaei, S.M., Sahimi, M., Rahimi Tabar, M.R.: *J. Stat. Mech.* (2008) P03016
44. Somfai, E., Roux, J.-N., Snoeijer J., H., Hecke, M.V., van Saarloos, W.: *Phys. Rev. E* **72**, 021301 (2005)
45. Sahimi, M.: *Comput. Sci. Eng.* **5**(4), 75 (2003)
46. Nussenzveig, H.M.: *Causality and Dispersion Relations*. Academic, New York (1972)
47. Aström, J., Kellomäki, M., Alava, M., Timonen, J.: *Phys. Rev. E* **56**, 6042 (1997)
48. Manshoor, P., Saberi, S., Sahimi, M., Peinke, J., Pacheco, A.F., Rahimi Tabar, M.R.: *Phys. Rev. Lett.* **102**, 014101 (2009)
49. Vaez Allaei, S.M., Sahimi, M.: *Phys. Rev. Lett.* **96**, 075507 (2006)